New benchmark problems for validation and verification of incompressible multi-fluid flows based on the improved Volume-Of-Fluid (VOF) method

Faroogh Garoosi*, Tew-Fik Mahdi

Department of Civil, Geological and Mining Engineering, Polytechnique Montreal, University of Montreal Campus, 2900 boul. Edouard-Montpetit, Montreal, QC H3T 1J4, Canada

Corresponding author: faroogh.garoosi@polymtl.ca,

Second author: tewfik.mahdi@polymtl.ca

Abstract

The present work describes the application of the improved Volume-Of-Fluid (VOF) method for the accurate capturing of phase interfaces in the problems of three-fluid bubble rising, water/oil droplets impacting onto wetted beds, three-fluid Rayleigh-Taylor Instability and merging of two rising bubbles, aiming to establish powerful benchmarking tools for validation of existing numerical models and code verification problems. To this end, an enhance version of the VOF model is exploited where a novel third-order TVD convection scheme is utilized for the discretization of convection terms in the Navier-Stokes and transport equations while the combination of the implicit non-iterative PISO and classical SIMPLER algorithms (PISOR) is applied for the treatment of the pressure-velocity coupling and acceleration of the iteration process in the Poisson equation. A series of canonical test cases including dam break over a dry bed, single and double rising bubbles, two-phase Rayleigh-Taylor Instability are considered to verify the performance and accuracy of the numerical method. The obtained results vividly demonstrate the superiority and versatility of the improved VOF model over the classical Eulerian and Lagrangian methods in handling multiphase flows with relevant breaking and fragmentation. Moreover, it is found that, the standard version of Lagrangian SPH models can

not accurately address the problem of interface smearing, and thereby characterizing by noisy pressure distribution.

Keywords: TVD convection scheme; Hybrid PISOR algorithm; Multi-fluid flows; PLIC-VOF method; Droplet impacting; Bubble rising;

Nomenclature

C_φ	Interface compression coefficient
F_g	gravity force
F_{ST}	surface tension force
g	Gravitational acceleration, ms^{-2}
H	enclosure height, m
L	Length of the enclosure (m)
$\mathbf{n}$	interface normal vector
p	pressure, Nm^{-2}
P	dimensionless pressure
t	time (s)
t^*	dimensionless time, ($t\alpha/H^2$)
u,v	velocity components, ms^{-1}
$\boldsymbol{u}_R$	artificial compressive velocity, ms^{-1}
Re	Reynolds number
U, V	Dimensionless velocity components
x,y	Cartesian coordinates, m
X, Y	Dimensionless Cartesian coordinates
We	Weber number

Greek symbols

μ	dynamic viscosity, kg m^{-1} s^{-1}
ν	kinematic viscosity, m^2s^{-1}
ρ	density, kg m^{-3}
φ	Volume fraction of the primary phase (phase 1)
λ	Volume fraction of the secondary phase (phase 2)
γ	Volume fraction of the third phase (phase 3)
k	curvature of interface
σ	interfacial tension coefficient
ψ	stream function($=-\int_{Y_0}^{Y} U\partial Y+\psi(X,Y_0)$)

Subscripts

L	Lighter fluid
H	Heavy fluid
M	Middle fluid

1. Introduction

The numerical approximation of immiscible multiphase flows with complex interfacial rheology has attracted substantial attention during the last two decades [1]. These interfacial phenomena are ubiquitous in many industrial and engineering applications such as evaporation and condensation [2], sloshing and flooding events [3,4], nuclear and chemical reactors [5], fluidized bed [6], liquid vaporization [7], combustion and fuel atomization [8,9]. In recent years, a considerable amount of research efforts have been devoted to the development of sophisticated mathematical techniques, applicable in the whole range of multi-fluid and multiphase flow configurations. Being the mainstream approaches, Level-Set (LS) and Volume-Of-Fluid (VOF) pioneered by Sussman et al. [10] and Hirt et al. [11] as the two most commonly cited methods

have been widely utilized to understand the underlying physics behind the multiphase flows in diverse fields. Given the pros and cons of each model, VOF and LS have been extensively employed to investigate a broad range of engineering problems such as bubble rising/nucleation [12–14], Rayleigh-Taylor Instability [15], dam failure phenomena [16–18], droplet impact on wet and dry surfaces [19–22], metals processing [23], just to mention a few. However, the results of Kumar et al. [24] and Scapin et al. [25] show that, despite the proven successes of aforementioned *interface-capturing* techniques over the traditional *front-tracking* [26] and *two-fluid* [27] approaches in handling complex multiphase processes, these methods are recognized by some numerical deficiencies such as violation of mass conservation principle, excessive computational smearing, inaccuracy in calculation of surface tension force, unphysical pressure/velocity fluctuations across the physical discontinuities, spurious growth of interface thickness arising from strong flow-to-grid skewness, and high CPU/memory computational cost when they come to solve Pressure-Poisson Equation (PPE). These drawbacks in turn can jeopardize the reliability of the numerical models and hinder their further applications as means of CFD tools. To be more precise, the former approach (LS) benefits from the smoothened Heaviside and Dirac Delta functions to introduce a narrow transition region for quantitative description of jump discontinuity and determine its geometrical information which are essential factors for approximating the surface tension effects [28]. Hence, the LS method can sometimes be regarded as a direct interface tracking technique where an explicit signed distance function (or step function) is utilized to control the thickness of the interface, making it conceptually simple and relatively easy to program [29]. However, this method suffers from loss of mass which can immensely compromise the accuracy of simulations especially when it comes to describe the highly deformed interfaces with coalescence and break-up events. Similar observations were also

reported by Lyras et al. [30] who used the hybrid Coupled-Level-Set-Volume-Of-Fluid (CLSVOF) approach to simultaneously circumvent the problems of mass inconsistency and loss of geometrical information. However, Lima et al. [21] highlighted that, the implementation of CLSVOF demands high computational effort and its efficiency comes at the cost of code complexity especially when it will be applied to the three-dimensions or non-orthogonal meshes. On the contrary, an alternative VOF model exhibits good mass conservation and uses the auxiliary advection equation (i.e. color function) to mark the phase interface in the entire computational domain [31]. In light of its implicit advantages in capturing complex topological changes of the interfacial problems, the VOF has become the predominant approach used by open-source and commercial CFD software packages [32]. Nevertheless, the results of Malgarinos et al. [33] reveal that, the standard VOF is characterized by some crucial drawbacks such as (1) undesirable interface smearing [34], (2) unphysical pressure oscillations near the contact discontinuities [35], and (3) poor level of accuracy in estimating the interface curvature and surface tension force [36]. These drawbacks in turn make the model virtually impractical for real-life cases involving interface merging, stretching, twisting and folding. During the past decades, an enormous amount of research has been conducted to tackle the above challenging problems and enhance the performance of the standard VOF model for solving hyperbolic conservation laws.

To counteract the first drawback and suppress false-diffusion errors, two basic methodologies are typically followed in the literature namely (1) implementing high-resolution bounded differencing schemes (HRS) and (2) utilization of Artificial Compression Technique (ACT). To minimize the errors caused by the numerical oscilation, Ami Harten [37] introduced the concept of Total Variation Diminishing (TVD) schemes which is able to provide satisfactory resolution

in the close proximity of the steep gradients region without generating spurious undershoots or overshoots oscillations in comparison with the conventional unbounded oscillatory schemes such as QUICK and Fromm [38]. Motivated by work of Ami Harten [37], many scholars have proposed different conservative differencing schemes to reconcile solution accuracy and numerical consistency (i.e. MINMOD, Van Leer, CICSAM, SMART, MUSCL) but all turn out to be too diffusive [39]. Recently, Garoosi et al. [40] proposed a novel third-order oscillation-free scheme to satisfy a convection-boundedness criterion. They numerically demonstrated that the newly constructed monotone TVD scheme is highly non-diffusive and can successfully retrieve the geometrical details of the interfaces. Moreover, they concluded that, their scheme can offer a notable compromise between accuracy and stability, making it more suitable for convection-dominated flows. The second alternative strategy attempts to compress interface region artificially through embedding an additional term into the advection equation. This idea was originally suggested by Heyns et al. [41] and then was successfully adopted by other researchers to tackle the problem of interface dispersing/wrinkling in modelling of the single rising bubble [42], slug flow regimes [43] and cavitation inside the diesel engine [44]. In the same context, the results of Garoosi et al. [40] showed that, the combination of the two aforementioned remedies (i.e. HRS & ACT) results in a more realistic simulations and will be a real benefit for any type of VOF predictions.

Referring to the second drawback, in order to suppress the pressure/velocity oscillations across the interface and improve the mass and momentum conservations in the incompressible fluid flows, Kim et al. [45], Tretola et al. [46] and Bruno et al. [47] suggested the use of PIMPLE algorithm (available in OpenFOAM® platform). However, a comprehensive review conducted by Wang et al. [35] revealed that, this pressure-based solver is computationally expensive as it

requires treating an additional iterative SIMPLE loop. To address this deficiency and speed up convergence rate of implicit iterative solver, Garoosi et al. [40] designed a novel hybrid semi-iterative PISOC algorithm where the SIMPLE algorithm [48] as a first part of the standard PISO algorithm [49] was replaced by the Two-step projection model [50]. They discovered that, the modified PISOC algorithm is computationally more efficient than the PIMPLE and is capable of alleviating nonlinear oscillations without any compromise of robustness.

Finally, as outlined before, the third major challenge associated with VOF method lies in achieving an accurate reconstruction of the interface and calculating its curvature. Fundamentally, an early study to circumvent this problem may be traced back to the previous work of the Youngs [51,52] who established the notion of Piecewise Linear Interface Calculation (PLIC) where a series of straight lines perpendicular to the gradient of volume fraction is utilized for the accurate imposition of the surface tension effects. However, Pilliod et al. [36] mathematically showed that, Youngs' method in nature is restricted to the first-order of accuracy and cannot exactly resolve all linear interfaces. As an alternative approach, he developed the second-order iterative ELVIRA technique where the orientation is to find the optimum inclined segment for minimizing reconstruction errors. This technique was then coded and utilized by Garoosi et al. [40] for the numerical simulations of dam break flow over dry and wet beds. They pointed out that, the advantage of this technique lies in its ability to handle arbitrarily shaped interfaces and to cope with abrupt topological changes.

In the light of the above literature survey, one can deduce that, the three crucial shortcomings associated with the standard VOF model have been systematically addressed in the previous work of Garoosi et al. [40]. However, it is obvious that further validations may be required prior to implementing it to a more complex interfacial flows. Thus, the first goal of the present work is

to further assess the performance and capability of the enhanced version of VOF model in handling multi-fluid flows with interface coalescence or rupture. To serve this purpose, four extra challenging benchmark cases including dam-break flow over the dry bed, single and double bubble(s) rising, two-fluid Rayleigh-Taylor Instability are selected and reproduced by means of the improved VOF model. In the second stage, the verified numerical model is employed to investigate four challenging engineering problems namely: three-fluid bubble rising, merging of two rising bubbles, water/oil droplets impacting onto the wetted beds, and three-fluid Rayleigh-Taylor Instability problems, aiming to establish up-to-date benchmarking tools for validating CFD tools. To the best of author's knowledge, such challenging test cases have not been reported in the published literature. The obtained results are presented in separate sub-sections and discussed in details.

2. Problem statement and governing equations

The schematic view of the computational domains related to twelve different physical models with coordinates and boundary conditions are sketched in Fig. 1. Since, the present study is a continuation of the previous work of Garoosi et al. [40], in the first step, four extra canonical problems namely two-fluid dam break flow, single/double rising bubble(s) and two-fluid Rayleigh-Taylor Instability (cases 1 to 4) are employed to further verify the performance and capability of the improved VOF model in handling multi-fluid flow problems. In the second step, four new benchmark solutions namely three-fluid Rayleigh-Taylor Instability (cases 5 to 7), three-fluid rising bubble (case 8), merging of two rising bubbles (cases 9 and 10) and water/oil droplets impacting onto wet beds (cases 11 and 12) are introduced and analyzed systematically, aiming to establish up-to-date benchmarking tools for validating CFD simulations. All simulations are performed in the Fortran 90 programming language and the developed code was

compiled using the Intel® Visual Fortran Compiler 19.0. The governing equations (i.e. continuity, momentum and volume fraction) for the Newtonian, laminar and incompressible multiphase flows in the Eulerian description can be written as follows [39,53]:

$$\frac{\partial \rho}{\partial t}+\frac{\partial \rho u}{\partial x}+\frac{\partial \rho v}{\partial y}=0, \tag{1}$$

$$\frac{\partial \rho_m u}{\partial t}+\frac{\partial \rho_m uu}{\partial x}+\frac{\partial \rho_m vu}{\partial y}=-\frac{\partial p}{\partial x}+[\frac{\partial}{\partial x}\mu_m(\frac{\partial u}{\partial x})+\frac{\partial}{\partial y}\mu_m(\frac{\partial u}{\partial y})]+F_{ST} \tag{2}$$

$$\frac{\partial \rho_m v}{\partial t}+\frac{\partial \rho_m uv}{\partial x}+\frac{\partial \rho_m vv}{\partial y}=-\frac{\partial p}{\partial y}+[\frac{\partial}{\partial x}\mu_m(\frac{\partial v}{\partial x})+\frac{\partial}{\partial y}\mu_m(\frac{\partial v}{\partial y})]+\rho_m g+F_{ST} \tag{3}$$

$$\frac{\partial \varphi}{\partial t}+\frac{\partial \varphi u}{\partial x}+\frac{\partial \varphi v}{\partial y}+\nabla\cdot(\varphi(1-\varphi)\mathbf{u}_R)=0 \tag{4}$$

$$\frac{\partial \lambda}{\partial t}+\frac{\partial \lambda u}{\partial x}+\frac{\partial \lambda v}{\partial y}+\nabla\cdot(\lambda(1-\lambda)\mathbf{u}_R)=0 \tag{5}$$

$$\varphi+\lambda=1 \text{ or } \varphi+\lambda+\gamma=1 \tag{6}$$

In the above equations, u and v are the velocity components in x and y-directions while the variables g, p and t denote gravity acceleration, pressure and time, respectively. ρ_m and μ_m are density and dynamic viscosity of working fluids which can be computed through the φ-, λ- and γ-weighted average of phases in each grid cell as [54]:

$$\rho_m=\varphi\rho_1+(1-\varphi)\rho_2 \tag{7}$$

$$\mu_m=\varphi\mu_1+(1-\varphi)\mu_2 \tag{8}$$

$$\rho_m=\varphi\rho_1+\lambda\rho_2+(1-\lambda-\varphi)\rho_3 \tag{9}$$

$$\mu_m=\varphi\mu_1+\lambda\mu_2+(1-\lambda-\varphi)\mu_3 \tag{10}$$

where Eqs. (7)-(8) are utilized for calculating the density and viscosity of two-fluid flow problems whereas Eqs. (9) and (10) are employed to estimate the fluid properties in the three-phase problems where the subscripts 1, 2 and 3 indicate the fluid-components under consideration. The last term in Eqs. (2) and (3) represent the contribution of the surface tension

force to the momentum which acts only in the vicinity of the physical discontinuity ($0<\varphi<1$, $0<\lambda<1$ and $0<\gamma<1$) based on the Continuum Surface Force (CSF) model introduced by Brackbill et al. [55] as:

$$F_{ST,\varphi}=\sigma_{\varphi}k_{\varphi}\nabla\varphi,$$
$$F_{ST,\lambda}=\sigma_{\lambda}k_{\lambda}\nabla\lambda, \tag{11}$$

In the above equation, σ is the interfacial tension between fluid phases and k stands for the curvature of interface which can be approximated by [56]:

$$k_{\varphi}=-\nabla\cdot\mathbf{n}_{\varphi}=-\nabla\cdot(\frac{\nabla\varphi}{|\nabla\varphi|}),$$
$$k_{\lambda}=-\nabla\cdot\mathbf{n}_{\lambda}=-\nabla\cdot(\frac{\nabla\lambda}{|\nabla\lambda|}), \tag{12}$$

$$\mathbf{n}_{\varphi}=\frac{\vec{n}_{\varphi}}{|\vec{n}_{\varphi}|},\ \vec{n}_{\varphi}=\nabla\varphi,$$
$$\mathbf{n}_{\lambda}=\frac{\vec{n}_{\lambda}}{|\vec{n}_{\lambda}|},\ \vec{n}_{\lambda}=\nabla\lambda, \tag{13}$$

where $\mathbf{n}$ denotes interface normal vector which is non-zero only at the interface. The last terms ($\nabla\cdot(\varphi(1-\varphi)\mathbf{u}_R)$ and $\nabla\cdot(\lambda(1-\lambda)\mathbf{u}_R)$) in the transport equations (i.e. Eqs. (4) and (5)) are the Artificial Compression Term (ACT) [41,42] which helps in suppressing interface smearing due to false diffusion errors. Note that, the existence of $\varphi(1-\varphi)$ and $\lambda(1-\lambda)$ scaling in the aforementioned equations ensures that the ACT is activated only in the interface region. $\mathbf{u}_R$ is the compressive velocity to compress the interface which can be formulated based on maximum velocity magnitude and gradient of volume fraction field within the grid cell as [43,44]:

$$\mathbf{u}_{R\varphi} = C_{\varphi}\left|\vec{u}\right|\mathbf{n}_{\varphi} = C_{\varphi}\left|\vec{u}\right|\frac{\nabla\varphi}{\left|\nabla\varphi\right|},$$

$$\mathbf{u}_{R\lambda} = C_{\lambda}\left|\vec{u}\right|\mathbf{n}_{\lambda} = C_{\lambda}\left|\vec{u}\right|\frac{\nabla\lambda}{\left|\nabla\lambda\right|}, \tag{14}$$

The coefficient $C_{\varphi} = 0.5$ is a scalar parameter which determines the strength of interface compression and is bound in the range of $0 \le C_{\varphi} \le 2$ [57,58].

3. Numerical methodology

The mass, momentum and volume fraction equations (Eqs. 1-5) are discretised using the finite volume approach on the uniform staggered grid arrangement where scalar variables including pressure, density and volume fraction of fluid phases are evaluated at the centre of control volumes whereas velocity components are centred around the cell faces [48]. The second-order central differencing scheme and three-time-levels scheme (second-order backward) are employed for the discretisation of diffusion and transient terms in the governing equations [59]. In order to overcome the problem of numerical diffusion errors and maintain the sharpness of the interface in multi-fluid flows, the third-order TVD convection scheme proposed by Garoosi et al. [40] is adopted for the treatment of the advection terms in the Navier-Stokes and transport equations. Furthermore, the combination of the classical PISO and SIMPLER algorithms (PISOR) is used to handle the pressure-velocity coupling and circumvent the problem of spurious pressure/velocity fluctuation adjacent to the physical discontinuity in unsteady incompressible multiphase flows. Finally, for the accurate imposition of the surface tension force, the Efficient Least squares Volume-of-fluid Interface Reconstruction Algorithm (ELVIRA) pioneered by Pilliod et al. [36] is coded and utilized for the calculation of the interface curvature. For the sake of brevity, detailed derivations of the TVD bounded convection

scheme, PISOR algorithm and ELVIRA technique are omitted here, but interested readers can refer to previous work of Garoosi et al. [40].

4. Validation and verification of the VOF model

To further demonstrate the accuracy and consistency of the improved VOF model in dealing with multi-fluid flows with moving interfaces, four different challenging benchmark problems such as dam break over a dry bed, single and double rising bubbles, two-fluid Rayleigh-Taylor Instability are numerically reproduced in this section. The transient evolution of each canonical test case is presented in forms of volume fraction, velocity and pressure contours and obtained results are discussed in details.

4.1.Dam break over a dry bed (Case 1)

The detailed layout of the small-scale experimental prototype of classical dam failure problem is illustrated in Fig. 1. This canonical test case was originally conducted by Lobovský et al. [60] and then was numerically analyzed by Zhang et al. [61], Gong et al. [62], Liu et al. [63], Kashani et al. [64], Daly et al. [65] and Asai et al. [66]. As it can be seen, the simulation is carried out in a rectangular flume with dimensions of $L = 3.22\,m$ long and $D = 2.2\,m$ deep where a volume of water ($W = 1.2\,m$ and $H = 0.6\,m$) with physical properties of $\mu_{Water} = 855\times10^{-6}\,kg\,m^{-1}s^{-1}$, $\rho_{Water} = 997\,kgm^{-3}$ and $\sigma = 0.071\,Kgs^{-2}$ is initially confined in the upstream area. The rest of the domain is occupied by air as a secondary phase ($\mu_{Air} = 184\times10^{-7}\,kg\,m^{-1}s^{-1}$, $\rho_{Air} = 1.0\,kgm^{-3}$). The time histories of impact pressure variations on the right-hand vertical wall are monitored by three virtual sensors deployed at points $h_{R1} = 0.006\,m$, $h_{R2} = 0.03\,m$ and $h_{R3} = 0.16\,m$ while the temporal evolution of the water level heights is measured at three distinct locations ($l_1 = 0.6\,m$,

$l_2 = 2.228\,m$ and $l_3 = 2.725\,m$). The calculation is performed on the regular grid system of 537×367 and predicted results in forms of the time evolution of the position/orientation of surge-wave front, free-surface profile, together with the snapshots of the pressure and volume fraction contours at different non-dimensional time instants ($T = t\sqrt{g/H}$) are portrayed in Figs. 2-4. It can be seen from Fig. 2 that, after the instantaneous removal of virtual barrier, the water column collapses and spreads over the dry bed as a surge wave until the water front hits the downstream boundary at $T = t\sqrt{g/H} \approx 2.5$ where first peak pressure takes place ($P_{\max,R1} = 2.250$, $P_{\max,R2} = 1.759$) over a duration less than 0.005T. However, after impinging onto the rigid right wall, due to the inertial effects, the stress wave reflects upward and propagates vertically until it reaches its maximum position at T=4.307. An interesting point is that, the maximum runup position of the ascending jet is approximately twice of its initial water depth at the dam site ($y_{\max} \approx 2H = 1.2\,m$) which is compatible with numerical and experimental findings of Colagrossi et al. [67] and Lobovský et al. [60]. As time passes, the rising jet slows down and starts to reverse in form of the plunging wave breaker, giving rise to the formation of a counter-clockwise vortex and abrupt change in the free-surface pattern (concave shape) adjacent to the right wall. As time further progresses, the amplitude and strength of the reverse plunging wave increase and consequently the appearance of air-cavity structure becomes more prominent. The newly developed stress wave eventually impact the forward face of advancing water surface below, resulting in the occurrence of the second peak pressure at $x = 2.62\,m$ and T=6.22. From the flow-visualization results of Fig. 2, one can observe that by this mechanism, the air is trapped by the swirling wave crest at the commencement of the shock pressure, forming a large air-cushion structure propagating in the upstream area. Shortly after the incident jet impacts the underlying

wetted bed, it starts to rebound from the main body at an angle with the bottom, establishing the second plunging jet at $6.22 \le T$.

The qualitative comparisons of the predicted results with numerical data and laboratory measurement of Zhang et al. [61], Liu et al. [63], Kashani et al. [64], Daly et al. [65], Asai et al. [66] and Lobovský et al. [60] in Figs. 3-5 demonstrate that, the overall features of the dam break flow in terms of collapsing, spilling, surging, and plunging breaking are satisfactory captured and reproduced by the improved VOF model. More precisely, it could be noticed that, the maximum runup position of the ascending jet along the vertical end wall during the time period of $2.750 \le T \le 4.783$ and the peak impact pressure acting on the bottom wall generated by plunging breaker wave are accurately estimated and captured by the present numerical method. However, it is evident that there is small discrepancy between the outcomes of the present model and those obtained by the classical Lagrangian SPH model which can be attributed to the existence of the some crucial shortcoming associated with SPH method such as smoothing errors, particle clustering (i.e. tensile instability) and low order-order of accuracy of differencing schemes [68]. Another reason can be traced back to the absence of secondary phase (i.e. air) in the numerical results of Zhang et al. [61], Liu et al. [63], Kashani et al. [64] which in turn can immensely influence the overall hydrodynamic behavior of the dam-break flow and reliability of the numerical simulation.

4.2.Single bubble rising (Case 2)

To further demonstrate the performance and accuracy of the proposed VOF model, the simulation of 2D single bubble rising in quiescent column of water ($\mu_H = \sqrt{2}/20\ kg\, m^{-1} s^{-1}$, $\rho_H = 100 kgm^{-3}$) is carried out here. As depicted in Fig. 1, the initial configuration is set to be

identical with numerical study of Zhao et al. [69] where a circular bubble ($\mu_L = \sqrt{2}/2000\ kg\, m^{-1}s^{-1}$, $\rho_L = 1.0 kgm^{-3}$) with a diameter $D = 2R = 0.5m$ is positioned at ($0.5H$, $0.37H$) in a $[1.0H, 1.62H]$ rectangular container with $H = 1.0m$ being the width of the enclosure. According to the aforementioned parameters and fluid properties, the density and viscosity ratios between dense and light fluids reach up to $\rho_H/\rho_L = 100$ and $\mu_H/\mu_L = 100$, respectively. The surface tension coefficient is $\sigma = 2.0\ Kgs^{-2}$ and the gravity acceleration is set to be $g = 4.0ms^{-2}$, giving rise to the Reynolds and Weber numbers equal to $\mathrm{Re} = \rho_H D\sqrt{Dg}/\mu_H = 1000$ and $We = \rho_H gD^2/\sigma = 50.0$. The no-slip boundary condition is imposed on both vertical and horizontal walls. The VOF snapshots of bubble evolution at some typical time instants ($T = t\sqrt{g/R}$) is displayed in Fig. 6 and compared with numerical results of Zhao et al. [69]. Generally, in this case, due to the extremely high Reynolds number and density contrast, the bubble shape undergoes significant deformation as it ascends upward in the opposite direction of gravity. It can be seen that in the early stages of the rising process, due to the upwelling water motion below the bubble, it turns into the horseshoe like structure ($0 \le T \le 2.0$). Subsequently, the cavity is gradually generated, and the bubble undergoes significant elongation (skirted bubble) until the breaking process initiates ($2.0 < T \le 4.0$). During the time-period of $4.0 < T \le 6.0$, due to the development of the wake region on the rear of the bubble, the bubble begins to transform into the mushroom-shaped structure. It is evident that by this mechanism, two small satellite droplets with thin filaments are generated and the formation of the filamentation phenomenon becomes more prominent. Later, due to the existence of the surface tension force and large interface curvature, the bottom tails of the bubble shrink upward, and the main body evolves into the cap-like structure. The qualitative and quantitative comparisons in

Figs. 6 and 7 vividly demonstrates that the maximum position of the bubble front conforms well to the previous results of Zhao et al. [69] and no interface smearing is found in the entire evolution process. This assertion is also well supported by Fig. 7 where an enlarged view of the grid spacing shows that, the interface thickness of the satellite bubble is successfully controlled and limited to the maximum 2-3 grid cells during the rising process.

4.3.Merging of two rising bubbles (Case 3)

Temporal evolution of buoyancy-driven merging of two rising bubbles with the same density and viscosity introduced by Grenier et al. [70] in the context of Lgrangian particle methods (SPH) is numerically reproduced here as a third challenging benchmark problem. As schematically shown in Fig. 1, two circular bubbles with nominal diameters of $D_1 = 2R_1 = 0.3\,m$ and $D_2 = 2R_2 = 0.2\,m$ are initially positioned along the vertical midline ($X = 0.5H = 0.5\,m$) of the container at $Y_1 = 0.65H = 0.65\,m$ and $Y_2 = 0.35H = 0.35\,m$, where $H = 10R_2 = 1.0\,m$ denotes the width of the computational domain. The densities of the lighter (i.e. bubbles) and heavy (i.e. surrounding phase) fluids are set to $\rho_L = 100\,kgm^{-3}$ and $\rho_H = 1000\,kgm^{-3}$, respectively, while the dynamic viscosities are set to $\mu_L = 0.078 kg\,m^{-1}s^{-1}$ and $\mu_H = 0.156 kg\,m^{-1}s^{-1}$, giving rise to the Reynolds and Bond numbers equal to $\mathrm{Re} = \rho_H R_2 \sqrt{gR_2} \big/ \mu_H = 633.0$ and $Bo = \rho_H g R_2^2 \big/ \sigma = 80.0$. No-slip boundary condition is set on horizontal walls whereas the free-slip boundary condition is applied on the vertical ones. The simulation is performed on the uniform structured mesh (500×750) and obtained results in forms of volume fraction and pressure contours are portrayed in Fig. 8 at eight different non-dimensional time instants ($T = t\sqrt{g/R_2}$). As shown in Fig. 8, both light bubbles ascend upward simultaneously under the action of buoyancy force while the surrounding

quiescent fluid starts to sink downward under the influence of the gravity force, resulting in a emergence of two opposite signed vortices within the container. This mechanism results in the development of a relatively lower pressure region in the wake of the leading bubble which causes the trailing bubble to be elongated and deformed into the dimpled-ellipsoidal shape. As time elapses, the bottom of the small bubble is stretched by the descending liquid jet while its front portion becomes narrower and steeper. It can be observed that as the smaller bubble penetrates further into the wake region of the larger bubble, the effects of surface tension force become more prominent and consequently the bubble detachment process initiates at the skirt of the lower bubble where the circulation current is less significant. Being in the wake of the upper bubble and aided by the surface tension force, two satellite bubbles are eventually formed on the edge of the lower bubble which undergo significant perturbations as two rising bubbles approach each other. As time proceeds, the leading bubble starts to cover and envelop the smaller one and the thin liquid film between them becomes thinner. Toward the end of the evolution, two bubbles merge with pronounced concentrations of vorticity. Shortly after their collision, the united bubble gets fragmented and splitted into two separate segments as it moves upward.

Qualitative comparison between results of the present study and those reported by Grenier et al. [70], Rezavand et al. [71], and Yang et al. [72] are portrayed in Fig. 9. It is evident that in spite of the small discrepancies between outcomes, the global behavior of the transport phenomenon in terms of the generation of the pinch and the subsequent detachment of drops together with the merging and splitting processes are satisfactory captured by the enhanced VOF method. However, similar to the previous section, it is apparent that, the calculated results are more consistent with the Level-Set solution than the pure Lagrangian particle model implemented by Grenier et al. [70] and Rezavand et al. [71]. These discrepancies can be partially attributed to the

order of the accuracy of governing operators adopted for the discretization of the velocity divergence, pressure gradient, diffusion terms and Pressure-Poisson equation in context of Euilerian and Lagrangian frameworks [73]. More precisely, the results of Agertz et al. [74], Bender et al. [75] and Sun et al. [76] showed that, the classical governing operators defined in SPH context (i.e. gradient, Laplacian and divergence) cannot accurately resolve multi-level vorticity and are inherently characterized by numerical dissipation/diffusion. These numerical shortcomings associated with SPH can lead to the substantial loss of accuracy and unphysical wake/pressure distributions around the bubbles interfaces. This assertion is consistent with results of Fig. 8 where the corresponding volume fraction and pressure contours obtained from the current work are symmetric and smooth without unphysical mixing. Furthermore, two enlarged snapshots of the detached daughter bubbles and liquid jet within the merged bubble in Fig. 10 reveal that, the thickness of the interface is efficiently controlled and limited to the maximum 2-3 grid cells which in turn confirms the robustness and capability of the proposed third-order bounded convection scheme in eliminating false-diffusion errors and retaining the sharpness of the density discontinuity. Finally, it should be noted that, the time variations of the maximum positions of the moving interfaces at two different sections (l_1=0.3 m and l_2=0.5 m) are presented in Fig. 10 as an additional information which has not been reported in the literature [70–72]. Finally, it is worth to mention that, the present canonical test case has been numerically investigated by Wen et al. [77] and Xu et al. [78] using, MPS, SPH and Level-set methods. However, for the sake of brevity, their data have not been reported in Fig. 9.

4.4.Two-phase Rayleigh-Taylor Instability (Case 4)

As highlighted before, the mixing of two immiscible incompressible fluids by single-mode Rayleigh-Taylor Instability (RTI) in the viscous regime can provide a good benchmark solution

to assess the accuracy and performance of the multi-fluid CFD models. Thus, the unsteady evolution of the classical two-phase RTI problem proposed by Farahbakhsh et al. [79] is reproduced here to verify the capability of the improved version of the VOF model in handling highly non-linear convection dominated multi-fluid flows. As schematically illustrated in Fig. 1, the simulation is performed in a rectangular domain of $[0,H]\times[0,2H]$ where $H=1m$ represents the width of the enclosure. To induce the RTI, a heavy fluid with nominal density and viscosity of $\rho_H=1.8\ kgm^{-3}$ and $\mu_H=0.001kg\,m^{-1}s^{-1}$ is initially positioned on top of the lighter fluid ($\rho_L=1.0\ kgm^{-3}$ and $\mu_L=0.001kg\,m^{-1}s^{-1}$) and the interface between two fluids is perturbed by function $y=1.0+0.1\times\cos(2\pi x)$. Since only two phases are involved in this canonical test case, Eq. (4) is implemented for capturing the position of the interface or calculating the volume fraction of the dense fluid (φ) while the formula ($\varphi+\lambda=1$) in Eq. (6) is used for the lighter fluid. No-slip boundary condition is applied on the surface of enclosure and the system is initially subjected to the gravitational acceleration with $\mathbf{g}=(0,-1)$. The density difference and flow regime are specified according to the Atwood and Reynolds numbers by $At=(\rho_H-\rho_L)/(\rho_H+\rho_L)=2/7$ and $\mathrm{Re}=\rho_H H\sqrt{gH}\big/\mu_H=1800$ with $U=\sqrt{gH}$ being the reference velocity. Based on the above pertinent parameters, the Froude number would be equal to unity ($Fr=(U\big/\sqrt{gH})=1$). The simulation is conducted on 350×700 grid resolution and comparison of predicted results with the corresponding previous data of Farahbakhsh et al. [79] are portrayed in Fig. 11 at different non-dimensional time instants ($T=t\sqrt{g/H}$). Generally, since the geometrical configuration and physical constituents of the medium with associated boundary conditions are symmetric with respect to the vertical axis, the heavy fluid falls down as a spike from the center, and the lighter fluid rises as bubbles adjacent to the vertical walls,

leading to the development of a pair of counter-rotating vortices within the container. This process causes the tails of the spike to roll up and bend inward while elongating vertically, giving rise to the observable mushroom-like structure. As time advances ($3 \le T \le 3.5$), owing to the presence of the viscous and shear forces, the interface undergoes significant twisting and deformation which signifies that the flow field is mainly governed by nonlinear Kelvin-Helmholtz Instability (KHI). As the dense fluid penetrates further into the light one ($3.5 < T \le 5.0$), the intensity of the fluid flow enhances and consequently some secondary spiral vortices appear within the enclosure. However, the interaction among the secondary eddies causes the interface to stretch and fold into very complex shape. This flow pattern is consistent by the emergence of the pair of kidney-shaped morphology in inner part of the interface. This interesting nonlinear behavior is also in accordance with numerical observations of Ding [80] who investigated 2D RTI problem in a relatively tall cavity. From the comparison between numerical outcomes, an excellent agreement can be observed, confirming that the complex topological changes in bubbly flow can still be successfully captured by proposed VOF method even at high Reynolds number ($\mathrm{Re} = 1800$). In addition, an enlarged portion of the kidney-shaped structure in Fig. 12 shows that, the interface thickness is well restricted to a maximum of 2-3 grid stencils which in turn highlights the accuracy and reliability of the proposed TVD convection scheme in minimizing undesirable effects of false diffusion errors. As an additional information, the maximum and minimum position of the interface is also provided in Fig. 12 which has not been reported in Ref [79].

5. Results and discussion

As outlined earlier, in this section, four new multi-fluid problems are introduced and analyzed using the verified VOF model, aiming to establish up-to-date benchmark solutions for CFD code

validation. The first challenging problem under consideration is the three-fluid Rayleigh-Taylor Instability (cases 5, 6 and 7) which is the extended version of the two-fluid RTI development. The second benchmark solution is the three-fluid single rising bubble located in the partially filled enclosure (case 8). The third challenging problem is the three-fluid rising bubbles where two circular bubbles with the same size but different densities are initially confined in the heavy quiescent fluid (cases 9 and 10). This problem is analogous to the well-known test case of merging of multiple parallel bubbles where the phenomenon so-called bubble coalescence or breakup process is likely to occur during the transient evolution. The last benchmark solutions encompass the liquid (water/oil) droplets impacting onto the wetted surfaces (oil/water layers) where the shock pressures due to slamming event is established in close proximity of the bottom wall. The knowledge about the droplets/bubbles/spikes trajectories and pressure/velocity variations during the impacting, merging (coalescence), splashing and plunging processes in cases 5-12 can increase the predictability of multi-fluid systems or even create an incentive to comprehend the underlying mechanisms behind the multiphase flows with moving interfaces. The predicted results in forms of volume fraction, velocity and pressure contours are presented in separate sub-sections and discussed in details.

5.1.Three-fluid Rayleigh-Taylor Instability (Cases 5, 6 and 7)

The nonlinear evolution of the three-fluid Rayleigh-Taylor Instability (RTI) is examined here as a first benchmark solution. As shown in Fig. 1, the computational domain in cases 5, 6 and 7 consists of three immiscible Newtonian viscous fluids with different properties which are initially confined in a rectangular enclosure with dimension of $[H, 2H]$ where $H = 1.0\,m$ represents the width of the container. The densities of the heavy, host and light fluids positioned

on the top, middle and bottom portions of the enclosure are set to $\rho_H = 4.0\ kgm^{-3}$, $\rho_M = 2.0\ kgm^{-3}$ and $\rho_L = 1.0\ kgm^{-3}$, respectively. No-slip Dirichlet boundary condition is imposed on both vertical and horizontal walls and the effect of surface tension force is ignored. The interfaces between two adjacent incompressible fluids are perturbed by sinusoidal functions defined as $y_1 = 2/3 + 0.05 \times \sin(kx)$ and $y_2 = 4/3 + 0.05 \times \sin(kx)$, respectively where $k = 2\pi/\lambda$ denotes the wavenumber. λ is the wavelength which is set to $\lambda = 1.0m$, $\lambda = 1/2m$ and $\lambda = 1/3m$, giving rise to the wavenumber to be equal to $k_{Case\,5} = 2\pi$, $k_{Case\,6} = 4\pi$ and $k_{Case\,7} = 6\pi$ in cases 5, 6 and 7, respectively. Similar to the previous problem, the instability is governed by two pertinent parameters namely Reynolds ($\mathrm{Re} = \rho_H H\sqrt{gH}/\mu_H = 420$) and Atwood ($At = (\rho_H - \rho_L)/(\rho_H + \rho_L) = 3/5$) numbers where $\mathbf{g} = 17.64\ ms^{-2}$ and $\mu_H = 0.04\ kg\,m^{-1}s^{-1}$ stand for the gravitational acceleration and dynamic viscosity of the dense fluid, respectively. Here, the kinematic viscosity is assumed to be identical for all fluids ($\nu_H = \nu_M = \nu_L = 0.01\ m^2s^{-1}$). Prior to the commencement of the simulations, it is worth to mention that, since three different fluids are engaged in this example, Eqs. (4) and (5) together with Eq. (6) (i.e. $\varphi + \lambda + \gamma = 1$) are utilized for approximating the volume fraction of each fluid while Eqs. (9) and (10) are employed to estimate their physical properties (ρ_m and μ_m). The calculations are performed on the uniform structured mesh (350×700) and the computed results at four different non-dimensional time instants ($T = t\sqrt{g/H}$) are depicted in Figs. 13-15. Generally, the morphological changes of the RTI evolution can be divided into three distinct stages. Stage 1 accounts for the linear regime where the RTI development is mainly governed by buoyancy and gravity forces and consequently the effects of drag and shear/viscose forces are negligible [81]. Stage 2 involves weakly/quasi nonlinear regime (or pseudo-terminal velocity regime) which is characterized by the emergence

of Kelvin-Helmholtz Instability (KHI) and the invigoration of shear velocity. Note that, the intensification of the shear stress at this stage is also accompanied by substantial twisting and deformation of the moving interfaces which manifest itself through the appearance of some secondary vortices at the tips and tails of the ascending/descending fluids (i.e. bubble-spike structures) [82]. Stage 3 encompass fully non-linear regime where the RTI evolution reaches its terminal condition and mixing process occurs at the constant velocity in a manner analogous to gradient diffusion [83]. Note that, the terminal condition is a situation in which the fluid flow reaches its steady velocity where all acting forces including drag, buoyancy, viscous and gravity are in hydraulic equilibrium. Based on the above description, it can be seen from Fig. 13 that, during the early stage of the RTI development ($0 \le T \le 1.26$), due to the existence of density gradient, the buoyancy force causes the lighter fluid (ρ_L) to move upward whereas the heavy fluid (ρ_H) descends downward under the action of the gravity force, resulting in the significant squeezing of the host fluid (ρ_M). At the same time, in order to ensure the mass continuity, the host fluid penetrates simultaneously into the adjacent dense and light fluids, leading to the appearance of multi-layered spike-bubble pairs within the container. Since, the rate of interpenetration between dense and host fluids in upper half of the enclosure is relatively identical to what happens between the host and lighter ones in the lower portion, the topological structures of the amplified perturbations remain almost symmetrical up-and-down with respect to the center of the enclosure in all cases, indicating the rigorous dominance of the buoyancy effects in the linear regime. This assertion is well supported by the symmetrical features of the velocity contours in Figs. 14 and 15. Beyond the initial stage ($1.26 < T \le 2.52$), however, the RTI undergoes considerable deformation which manifests itself through the establishment of some secondary rolling eddies on the sides of the spike-bubble structures. As highlighted before, in

these circumstances, viscosity and drag forces have moderate impact on the growth of the large-scale vortices. Note that, this flow pattern corresponds with the onset of the Kelvin-Helmholtz Instability (KHI) and pseudo-terminal velocity regime, accordingly. Furthermore, it is evident from Figs. 14 and 15 that, the transition from the linear flow regime to the quasi-nonlinear one during this time period is characterized by considerable augmentation in the flow intensity and the formation of inner rolled-up/rolled-down vortices. As time goes on ($2.52 < T \leq 3.402$), the motion of the fluids flow decelerates slightly and the symmetrical features of velocity and volume fraction contours (i.e. the reversal and amplification of spike-bubble structures) begin to die out. However, due to the non-linear interaction between smaller structures, the growth of the large-scale eddies is inhibited and consequently mixing process begins to come into the picture, indicating the inception of the fully-non-linear regime. It can be seen that, later stages of the evolution ($3.402 < T \leq 4.284$) is characterized by the significant degradation of the mushroom-like structures (upward/downward plumes) and the reduction of the flow intensity. This assertion is well supported by Figs. 14 and 15 where the rate of fluids movement along the vertical direction declines or shows oscillatory behavior whereas the velocity component in horizontal one increases continuously, proving the attenuation in the convection mass transfer and the intensification in mode of diffusion one. As expected at this stage, the interfaces along the two interacting fluids are further twisted and ultimately evolved into amorphous-like structures. However, a close inspection of the results in Figs. 13-15 demonstrates that by increasing the wavenumber from $k_{Case\,5} = 2\pi$ to $k_{Case\,7} = 6\pi$, the maximum velocity components and magnitude of mixing process decrease. This physical behavior may be attributed to the fact that, by increasing the wavenumber, the tangential velocity of moving interfaces decreases and consequently the destabilizing effect of shear flow declines due to the viscous effects. Similar

observation was also reported by Mankbadi et al. [84] who numerically showed that the growth rate of RTI enhances with increasing the wavenumber, but there exists an optimum value, beyond which growth rate starts to suppress or even quench with further increase in wavenumber. In the same context, the results of Morgan et al. [85] showed that by decreasing the wavelength of the perturbation (or for sufficiently short wavelength), the RTI development is suppressed and the viscous force becomes dominant over the shear velocity. These findings are also in accordance with the time histories of the fluids positions presented in Fig. 16. It is evident that, the minimum and maximum locations of the dense and light fluids in cases 5 ($k_{Case\,5} = 2\pi$) and 6 ($k_{Case\,6} = 4\pi$) are relatively close to each other whereas by increasing the wavenumber from $k_{Case\,6} = 4\pi$ to $k_{Case\,7} = 6\pi$, the fluids displacement decreases, suggesting that the interface disturbance can be stabilized for a wavenumber modulus larger than some threshold value. Finally, the overall examination of interfaces dynamics illustrates that, the global characteristics of the RTI evolution in terms of the emergence of spike-bubble structures and Kelvin-Helmholtz Instability are well captured by the improved VOF model without any unphysical interface smearing. The smooth variation of fluid color and velocity field during the RTI development vividly proves the robustness of the proposed PISOR algorithm in handling velocity-pressure coupling in incompressible multi-fluid flows with large topological changes.

5.2.Three-fluid rising bubble (Case 8)

Inspired by work of Pan et al. [86], the hydrodynamic characteristics and morphological changes of a single rising bubble confined in a partially filled container subjected to the gravitational acceleration is investigated as a second benchmark solution. The initial configuration is presented in Fig. 1. As schematically shown, the computational domain consists of a rectangular

enclosure with dimension of $[2.5H, 3.5H]$ where $H = 2R = 1.0m$ denotes the diameter of the circular bubble ($\rho_M = 400\ kgm^{-3}$ and $\mu_M = 8.0 kg\, m^{-1}s^{-1}$). The lower portion of the container is filled with Newtonian incompressible fluid with density and viscosity of $\rho_H = 1000\ kgm^{-3}$ and $\mu_H = 20 kg\, m^{-1}s^{-1}$ while the upper part is occupied with lighter fluid with physical properties of $\rho_L = 1.0\ kgm^{-3}$ and $\mu_L = 0.02 kg\, m^{-1}s^{-1}$, respectively. Similar to the numerical study of Pan et al. [86], in order to reach the highest interfacial topological changes, the effects of the surface tension force is ignored. The calculation is conducted on the uniform grid resolution of 450×630 and no-slip boundary condition is imposed on all solid walls. As sketched in Fig. 1, the bubble is initially positioned at $X = 1.25m$ and $Y = 1.4m$ surrounded by the heavy fluid with height of $L = 2.5m$. In the present work, the subscripts *L, M* and *H* represent the light, middle and heavy fluids, respectively. The bubble evolution is governed by Froude and Reynolds numbers given by $Fr = u/\sqrt{gH} = 1.0$ and $\mathrm{Re} = \rho_H H\sqrt{gH}/\mu_H = 210$ with $g = 17.62\, ms^{-2}$ and $u = \sqrt{gH}$ being the gravitational acceleration and reference velocity, respectively. Time evolution of bubble shape during the rising process at different non-dimensional time instants ($T = t\sqrt{g/H}$) is presented in Fig. 17. It can be seen that in the absence of the surface tension force, the bubble experiences strong deformations especially in the later stage where the detachment process occurs and two daughter bubbles are separated from the main body. More precisely, Figs. 17-19 reveal that, in the early stage of the buoyant motion ($0 \le T \le 1.848$), the bubble rises up from the midline of the enclosure while the dense fluid descends downward at both sides of the domain, leading to the emergence of two symmetric counter-rotating eddies within the enclosure. The corresponded velocity contours show that at this stage, the magnitude of both longitudinal and transverse velocities (*U*,*V*) increase and subsequently the bubble

deforms rapidly and evolves into the dimpled cap structure. However, as the bubble approaches the upper portion of the domain, due to the blockage effects of the free-surface area ($1.848 < T \leq 4.032$), the thickness of bubble in the vertical direction gradually declines and its diameter in the horizontal one increases, resulting in the formation of the dimpled ellipsoidal-cap structure. Inspection of Figs. 18 and 19 reveal that, this stage is accompanied by remarkable reduction in vertical velocity and the development of wake region behind the bubble. This mechanism causes the bubble to pierce from the bottom and turn into the shape of horseshoe. As a consequence, some secondary eddies are formed inside and outside of the bubble, indicating the inception of the Kelvin-Helmholtz Instability (KHI) along the moving interface. Note that, the onset of the KHI is accompanied by the termination of the piercing process (or indentation process) and the initiation of flattening/filamentation one. As time goes on ($4.032 < T \leq 5.208$), the intensity of the shear velocity enhances, thereby causing the bubble to elongate in the *x*-direction. It can be observed that as the skirted bubble stretches horizontally, the tails of the bubble begin to fold inward and exhibit strong non-linearity and deformation which can be attributed to the interactions between neighboring small eddies and the occurrence of the pseudo-terminal velocity regime. In the later stages of the evolution ($5.208 < T \leq 6.552$), sharp-edged filaments ultimately emerges and the lower portion of the bubble becomes thinner and thinner until the droplets detachment occurs. This yields a pair of smaller sidewise flow on the rear of the parent bubble which circulates around the child bubbles and manifests itself through the formation of some secondary tiny vortices. Fig. 18 and 19 reveals that, during this time period, both velocity components in *x*- and *y*-directions lessen and reach their terminal condition which implies that viscous and drag forces are sufficiently strong to sustain the shear velocity and buoyancy force at the bubble front.

The maximum and minimum positions of the bubble interface together with the zoomed-in view of the skirted bubble are depicted in Fig. 20. It is evident that during the rising process, the extreme position of the bubble front exhibits an oscillatory behavior which can be attributed to the blockage effects of the free-surface area and the elongation/broadening of the bubble tip in vicinity of the lighter fluid. On the other hand, the minimum position of the bubble initially increases during acceleration stage and then decreases during deceleration stage. This physical pattern is mainly attributed to the formation of mushroom-like vortex motions and wake region behind the bubble which causes two satellite droplets to be sucked toward the bottom wall. Finally, the enlarged portion of the bubble at T=5.208 shows that, the moving interface is smooth and free from numerical dissipation and smearing, affirming the robustness and performance of the proposed TVD scheme in suppressing false-diffusion errors.

5.3.Merging of two rising bubbles with different densities (Cases 9 & 10)

In this subsection, we aim to follow up our previous work and examine the transient evolution of merging of two rising bubbles with different densities but same diameters [87]. The geometric configurations of interest are depicted in Fig. 1. As schematically portrayed, the calculations in cases 9 and 10 are performed in the rectangular box with dimensions of $[1.5H, 2.5H]$ where $H = 1.0m$ denotes the reference length. Two circular bubbles with same diameters ($D_1 = D_2 = 2R_1 = 2R_2 = 0.6m$) are centered across the midline of the enclosure ($X = 0.75H = 0.75m$) at $Y_1 = 1.3H = 1.3m$ and $Y_2 = 0.6H = 0.6m$, respectively. The density and viscosity of the bubbles ($\rho_M = 500kgm^{-3}, \rho_L = 250kgm^{-3}$, $\mu_M = 10kg\,m^{-1}s^{-1}$, $\mu_L = 5kg\,m^{-1}s^{-1}$) and the surrounding fluid ($\rho_H = 1000kgm^{-3}, \mu_H = 20kg\,m^{-1}s^{-1}$) in cases 9 and 10 are chosen in a manner that the kinematic viscosity of working fluids becomes identical in all cases (

$\upsilon_H = \upsilon_M = \upsilon_L = 0.02 m^2 s^{-1}$). According to the aforementioned parameters and fluid properties, the Reynolds and Froude numbers may be defined as $\mathrm{Re} = \rho_H D_1 \sqrt{gD_1} \big/ \mu_H = 69.713$ and $Fr = U_0 \big/ \sqrt{gD_1} = 1.0$ where $\mathbf{g} = 9.0 ms^{-2}$ stands for the gravitational acceleration. Inspired by works of Pan et al. [86] and Li et al. [88] and Zhao et al. [69], in order to reach the highest rate of topological changes and bubbles deformations during their rising process, the surface tension force has not been included in the problem. The simulations are carried out on the uniform structured mesh 451×751 and no-slip boundary conditions are set on all rigid walls. The predicted results in forms of the volume fraction contour and velocity fields in both *x*- and *y*-directions are displayed in Figs. 21 to 23 at different non-dimensional time instants ($T = t\sqrt{g/D_1}$). As highlighted by Jávor et al. [89], Zawala et al. [90] and Malysa et al. [91], regardless of the presence or absence of the surface tension force, the morphological alterations and hydrodynamic behavior of the bubble motion in the initially static field can be classified into three well-separated stages namely: (1) the rapid acceleration and rectilinear rising, (2) quasi-terminal condition or deceleration stage, and (3) terminal velocity stage. More precisely, the first stage is characterized by the continuous ascending of the bubble(s) which manifests itself through the significant augmentation in the magnitude of the velocity components and fast deformation of the bubble(s) shape. This stage which is mainly governed by the buoyancy force is also accompanied by the simultaneous formation of the downwelling liquid jet adjacent to the rigid wall and upwelling liquid motion below the bubble which causes the circular bubble(s) to transform into the well-known dimpled cap (or horseshoe-like) structure. By this mechanism, the cavity gradually grows, and the bubble is progressively elongated, indicating the onset of the wake instability or even vortex shedding within the fluid domain. It is important to stress that,

the phenomenon so-called "*wake instability*" can be more pronounced in turbulence regime where some secondary eddies with different size are likely to emerge during the transport process [92]. In fact, the emergence of the vortex shedding causes the bubbles to travel in a zigzag or helical trajectory. Stage (2) encompasses quasi-terminal condition where the bubbles undergo remarkable deformation and deceleration under the influence of the drag and pressure gradient forces. In these circumstances, the interfaces experience severe stretching and twisting owing to the strengthening of the viscous shear stress along the moving interfaces and wake vortices behind both leading (upper) and trailing (lower) bubbles. This physical behavior is accompanied by a reduction in the diameter of the bubble in the vertical direction and its widening in the horizontal one. Note that, during this process, the shear forces induced by velocity gradient surrounding the bubble(s) may promote filamentation, generating a quasi-steady slender thread in rear of the parent bubble. In the third stage, bubble(s) reaches a steady state condition and move(s) at the constant velocity which is referred to as "*terminal velocity*". Consequently, no significant variations occur in the shape and fluidity of the bubble interface at this stage.

Based on the above description, one can observe from Fig. 21 that, driven by the buoyancy force, both bubbles in cases 9 and 10 ascend upward while the surrounding heavy liquid moves downward under the action of the gravity force to fulfill the need for the mass conservation. The corresponded velocity fields in Figs. 22 and 23 reveal that, during the early stages of the evolution ($0 \le T \le 2.323$), the intensity of the velocity components is amplified dramatically and a pair of counter-rotating vortices is established in the left and right halves of the enclosure, confirming the pure dominance of the buoyancy force. As anticipated, this period of acceleration is followed by the gradual transformation of the bubbles from circular shape into the dimpled

ellipsoidal cap. After the acceleration stage ($2.323 < T \leq 3.408$), however, the fluid flow enters the stage of asymptotic velocity alteration (i.e. decrease or increase) where the bubbles attain its maximum velocity. It can be seen that at this stage in both cases, the upper bubble sucks the lower one up and starts to envelop it, resulting in the collision and eventual merging of two bubbles. However, it is evident that the coalescence process of two rising bubbles is considerably affected by the densities of the leading and trailing bubbles ($\rho_M = 500 kgm^{-3}, \rho_L = 250 kgm^{-3}$). More precisely, since in case 9 the density of the upper bubble is higher than the lower one ($\rho_{Lower} < \rho_{Upper}$), the trailing bubble moves/deforms much faster than the leading bubble such that the rise velocity of the upper bubble in this case reaches its maximum value soon and begins to decline whereas the lower bubble keeps being accelerated until it catches up with the upper one. This suggests that, due to the small density difference between leading bubble and surrounding fluid ($\rho_M / \rho_H = 2$), the leading bubble in case 9 acts as a barrier, thereby hindering the upward movement of the lower bubble. As time elapses, the liquid film between two bubbles gets thinner and ultimately the coalescence process takes place. Contrary to case 9 in which the lower bubble is totally covered/swallowed by the upper one, due to the high density contrast between the leading bubble and surrounding liquid in case 10 ($\rho_L / \rho_H = 4$), the leading bubble is elongated vertically and evolved into the skirt-like structure while the trailing bubble takes the form of a mushroom shape (i.e. plume structure), indicating that the wake region induced by the upper bubble in case 10 is relatively weaker as compared to the previous case. This assertion is well supported by Fig. 23 where the magnitude of the velocity field in *x*-direction in case 10 is slightly higher than that of case 9 throughout the entire sequence of bubble evolution. However, similar to case 9, due to the resultant wake vortices, the trailing bubble is eventually dragged into the upper one and consequently the process of film thinning initiates. On the other hand, by

comparison of the predicted results in Fig. 21 between cases 9 and 10 one can observe that, the shape of bubbles in case 10 lies somewhere between the skirted and dimpled ellipsoidal cap structures whereas in case 9 the upper bubble has a tendency to totally embrace the lower one which can be ascribed to rise velocity, density differences and intensity of the resultant wake region between two bubbles in these cases. Taking these topological changes into consideration, one can conclude that, the early evolutionary history of rising bubbles with same densities ($\rho_{Lower} = \rho_{Upper}$) should be situated between two aforementioned cases. Toward the last stages of the computation ($3.408 < T \leq 4.647$), due to the significant intensification of the drag and viscous forces (i.e. shear stresses), the circulation current inside the bubbles decrease and consequently the deformation rate of the bubbles remains nearly unchanged, denoting the inception of the terminal condition. The corresponded velocity contours in Fig. 22 and 23 reveal that, the magnitude of the velocity components decrease and reach the steady constant value which indicates that the hydrodynamic balance between all acting forces on the rising bubbles (i.e. buoyancy, drag, gravity and viscosity) has been established. The time histories of the maximum position of the bubbles fronts in Fig. 24 show that the time variations of the lower bubble position in both cases is considerably higher than that of the upper one which can be attributed to the existence of the wake region behind the leading bubble. This mechanism causes the trailing bubble to experience a much lower drag force. However, a close inspection of the figure reveals that, the maximum position of the leading bubble in case 10 is slightly higher than that of case 9 which can be ascribed to higher buoyancy force acting on the upper bubble in this case ($\rho_{Upper} = \rho_L \ll \rho_H$). Finally, the global examination of Figs. 21-23 illustrates that both volume fraction and velocity fields across the material discontinuities are smooth without any

smearing, confirming the accuracy and consistency of the proposed PISOC algorithm and TVD convection scheme in alleviating the numerical oscillation/diffusion.

5.4. Water/oil droplets impacting on the wetted beds with finite thickness (Cases 11 & 12)

Liquid droplet interaction with dry and wet surfaces has attracted great attention in the recent years due to its wide applications in many industrial and environmental processes. Examples include spray cooling of turbine blades, rain falling in nature, chemical reactors, spray combustion in liquid-fueled, ink-jet printing, pesticide delivery and so on [93]. The fluid mechanics of spreading of a liquid droplet upon a solid surface has been investigated and well-documented by many scholars [94]. Despite many attempts, the mechanism of droplet collision with a wetted surface is not yet well understood and still remains elusive [95]. Thus, lack of information about the principles that govern the flow of such phenomenon has motivated us to establish this novel benchmark solution, aiming to provide detailed insights into the coalescence dynamic of droplet impact/deposition on the thin liquid film. The initial configurations of the problem (cases 11 and 12) under study are portrayed in Fig. 1. As schematically shown, the calculations in both cases are conducted in a rectangular container with the dimension of $[2H, H]$ where $H = 1.0\,m$ denotes the height of the enclosure. A circular drop with diameter of $D = 2R = 0.4\,m$ is centered across the midline of the enclosure at $X = H = 1.0\,m$ and $Y = 0.55H = 0.55\,m$. The initial depth of the wetted bed in both cases is $B = 0.2\,m$. Similar to the previous benchmark solutions, the subscripts *L, M* and *H* are assigned to the light ($\rho_L = 1.0\,kgm^{-3}, \mu_L = 0.001\,kg\,m^{-1}s^{-1}$), middle ($\rho_M = 500\,kgm^{-3}, \mu_M = 0.1\,kg\,m^{-1}s^{-1}$) and heavy ($\rho_H = 1000\,kgm^{-3}, \mu_H = 1.0\,kg\,m^{-1}s^{-1}$) fluids, respectively. By comparing cases 11 and 12, one

can found that, two cases are designed in a way that enables us to investigate the effects of density/viscosity of the droplet and a liquid layer on the resultant impact pressure and topological changes of the phenomenon. More precisely, in case 11 the physical properties of the middle and dense fluids are assigned to the droplet (ρ_M, μ_M) and wetted bed (ρ_H, μ_H) whereas these physical parameters are chosen for the wetted bed (ρ_M, μ_M) and droplet (ρ_H, μ_H) in case 12. The rest of the enclosure in both cases is filled by the lighter fluid (ρ_L, μ_L). The droplets are released at rest ($\mathbf{u} = 0\, ms^{-1}$) and the effects of the surface tension force is not taken into consideration. The no-slip wall condition is imposed on the rigid walls and the Reynolds and Atwood numbers are set as $\mathrm{Re} = D\sqrt{gD}/\upsilon_H = 792.36$ and $At = (\rho_H - \rho_M)/(\rho_H + \rho_M) = 1/3$ where $\mathbf{g} = 9.81\, ms^{-2}$ and $\upsilon_H = \upsilon_M = \upsilon_L = 0.001\, m^2 s^{-1}$ stand for the gravitational acceleration and kinematic viscosity of the fluids [96]. A sequence of droplets shape evolution at various time instants with corresponding pressure contours are depicted in Figs. 25 and 26. Generally, the hydrodynamic and morphological changes of liquid droplet impingement on wet surface can be divided into three distinct stages namely: (1) falling and coalescence stage where the first shock pressure occurs and the viscous force has minor influences on fluid flow, (2) spreading and propagating of impacting droplet where the phenomenon so-called wave breaking occurs and fluid flow is governed by inertia force, and (3) contracting or retracting stage where the volume of the droplet starts to move backward and surge to its initial position, resulting in the formation of tidal-like structure or plunging breaking wave within the computational domain [97]. Note that, regardless of the viscosity ratio between droplet and wetted surface, the first stage of the droplet collision is characterized by relatively large energy dissipation where the kinetic energy of the system is irreversibly converted into the shock pressure. In addition, the second and third stages are characterized by splashing of satellite droplets where the impacting droplet breaks into

smaller bouncing drops. Based on the above explanation one can observe that, at the early stages of impact process, the oil and water droplets in both cases descends downward under the influence of the gravity force until the tips of the droplets reach the wetted surface approximately at $t = 0.2\,s$ where the first impact pressure occurs. A further scrutiny of the pressure contours in Fig. 26, however, reveals that, the magnitude of the shock pressure in case 11 ($P_{\max} = 2.21$) is considerably lower than that of case 12 ($P_{\max} = 4.059$) which can be attributed to low density ratio between droplet and liquid film in this case ($\rho_{Droplet} / \rho_{Wetted\ bed} = \rho_M / \rho_H = 0.5$) as compared with case 12 ($\rho_{Droplet} / \rho_{Wetted\ bed} = \rho_H / \rho_M = 2.0$). This observation is in accordance with pressure variations recorded by sensor 1 installed at the impact point ($l_1 = 1.0\,m$) at $t = 0.2\,s$ as illustrated in Fig. 27. This numerical finding is also consistent with experimental data of Kim et al. [98] who showed that the droplets with larger impact inertia generates remarkably higher shock pressure than those with weaker inertia. Another interesting point which can be extracted from Fig. 27 is that, unlike the case 11 in which the pressure field decreases monotonically after the collision event, due to higher gravitational potential energy in case 12, the pressure value increases monotonically until it reaches the peak value ($P_{\max} = 5.102$) at $t = 2.28\,s$ [99]. As time advances, the circular droplets progressively evolve into the bell-shaped structure and the formation of plunging jets in both cases gets more prominent. It can be seen that as the droplets approach the bottom wall, the liquid film in both cases becomes thinner and the influence of potential energy on upward bulk motion and subsequent wave breaking increase. However, unlike the case 11 in which the oil droplet has a tendency to drift and slide on the wetted surface, the water droplet in case 12 penetrates more into the thin oily bed and settles near the bottom wall as illustrated in Figs. 25 and 27 (a). As time progresses, the amplitudes of plunging jets

augment and consequently the quasi-hydrostatic pressure field forms near the downstream end walls. The corresponded pressure fields in Fig. 26 illustrate that the enhancement in the hydrostatic pressure distribution continues until the plunging jets hit the end vertical walls where the second shock pressure forms on the bottom-left and bottom-right corners of the enclosure. However, due to the viscous effects and hydraulic resistances between interacting fluids, the momentum of the system decreases and subsequently the motion of droplets in the horizontal direction decelerate. It is evident that after spreading stage, the droplets start to recoil and travel toward the initial impact point. However, one can observe that depending on the density ratio between droplet and liquid film, different scenario in form of "floating" or "immersion" phenomenon may occur within the fluid domain. It can be seen that, due to the low density contrast in case 11 ($\rho_{Droplet}/\rho_{Wetted\ bed} < 1.0$), the oil droplet remains floating on the water surface whereas the water droplet in case 12 ($\rho_{Droplet}/\rho_{Wetted\ bed} > 1.0$) immerses within the oil pool and starts to be surrounded/enveloped by the overturning plunging jet, giving rise to much more complicated flow pattern in this case as illustrated in Fig. 25.

The overall examination of the predicted results in Figs. 25 and 26 demonstrates that, the global features of droplet impacting onto the liquid film in terms of partial coalescence, spreading behaviors, and recoiling stage are well simulated and captured by the enhanced VOF model. The smoothness of the fluids interfaces together with corresponding pressure fields in Figs. 25 and 26 vividly proves the capability and robustness of the proposed TVD scheme and hybrid PISOR algorithm in mitigating false-diffusion errors (or false scattering) and numerical oscillation in dealing with multi-fluid flows involving large interface deformation and topological changes (i.e. interface coalescence or rupture).

6. Conclusions

In the present work, four new benchmark solutions namely three-fluid bubble rising, merging of two rising bubbles, water/oil droplets impacting on the wetted beds, and three-fluid Rayleigh-Taylor Instability problems are introduced and examined numerically using the enhanced VOF model. To accomplish this objective, the performance and capability of the improved Volume-Of-Fluid (VOF) method are first demonstrated against four additional canonical multi-fluid problems such as dam-break flow over a dry bed, single bubble rising, merging of two rising bubbles, two-fluid Rayleigh-Taylor Instability. The verified VOF model is then utilized to investigate the aforementioned benchmark solutions, aiming to provide reliable and accurate databases for validation and verification of CFD tools. Based on the simulated results, the following conclusions may be drawn:

- It is found that, the proposed model allows accurate and consistent predictions of non-linear free-surface flows involving, plunging wave breaking, large slamming events, impact pressure and interface rupture/coalescence.
- It is found that, the proposed third-order TVD convection scheme can successfully address the problems of interface smearing and physical discontinuities in convection dominated-flows without generating spurious oscillations.
- The close-up snapshots of the moving interfaces in all cases vividly affirm the robustness of the proposed TVD bounded convection scheme in preserving interface resolution/boundedness and suppressing undesirable numerical diffusion arising from flow-to-grid skewness.
- The results show that, the standard Lagrangian SPH model fail to maintain the sharpness of the material discontinuities.

- The numerical simulations of three-fluid bubble rising and Rayleigh-Taylor Instability problems clearly demonstrate the capability of the improved VOF model in handling multi-fluid flows.
- The results reveal that, the utilization of hybrid PISOR algorithm leads to a more stable/consistent numerical solutions and provides smoother pressure/velocity fields across the physical discontinuities.
- The results show that in the case of the double rising bubbles, the size and intensity of the wake region behind the upper bubble has a considerable impact on the shape, trajectory and velocity of the lower bubble, as well as the intensity of the liquid jet surrounding them.
- The results show that, in the problem of three-fluid Rayleigh-Taylor Instability, by increasing the wavenumber of the perturbed interfaces, the rate of mixing process and intensity of the fluid flow decrease.
- The results show that, the temporal evolution of the merging of two rising bubbles can be remarkably affected by densities of the leading and trailing bubbles.
- The results show that, the morphological changes of the collision of falling oil/water droplets on the wetted surfaces can be significantly affected by the density ratio of the droplet and thin liquid film (wetted bed).

Supplementary material

In order to shed more light on the morphology and hydrodynamics behavior of simulated benchmark cases, twelve different animations are provided as supplementary material.

Declaration of Competing Interest

The authors declare that they have no known competing financial interests or personal relationships that could have appeared to influence the work reported in this paper.

Acknowledgment

This research was funded, in part, by a National Science and Engineering Research Council (NSERC) Discovery Grant for the co-author Tew-Fik Mahdi, application No: RGPIN-2021 03272.

CRediT authorship contribution statement

Faroogh Garoosi: Conceptualization, Methodology, FORTRAN Code development, Validation, Visualization, Writing-Original Draft.

Tew-Fik Mahdi: Supervision, Funding acquisition, Validation, Writing-Review & Editing.

References

[1] G. Tryggvason, R. Scardovelli, S. Zaleski, Direct numerical simulations of gas–liquid multiphase flows, Cambridge University Press, 2011.

[2] L. Bureš, Y. Sato, Direct numerical simulation of evaporation and condensation with the geometric VOF method and a sharp-interface phase-change model, Int. J. Heat Mass Transf. 173 (2021) 121233.

[3] C. Zhang, J. Tan, D. Ning, Machine learning strategy for viscous calibration of fully-nonlinear liquid sloshing simulation in FLNG tanks, Appl. Ocean Res. 114 (2021) 102737.

[4] R. Saghi, S. Hirdaris, H. Saghi, The influence of flexible fluid structure interactions on sway induced tank sloshing dynamics, Eng. Anal. Bound. Elem. 131 (2021) 206–217.

[5] L.D. Silvi, D.K. Chandraker, S. Ghosh, A.K. Das, Understanding dry-out mechanism in rod bundles of boiling water reactor, Int. J. Heat Mass Transf. 177 (2021) 121534.

[6] M. Vångö, S. Pirker, T. Lichtenegger, Unresolved CFD–DEM modeling of multiphase flow in densely packed particle beds, Appl. Math. Model. 56 (2018) 501–516.

[7] J. Palmore Jr, O. Desjardins, A volume of fluid framework for interface-resolved simulations of vaporizing liquid-gas flows, J. Comput. Phys. 399 (2019) 108954.

[8] F. Giussani, F. Piscaglia, G. Saez-Mischlich, J. Hèlie, A three-phase VOF solver for the simulation of in-nozzle cavitation effects on liquid atomization, J. Comput. Phys. 406 (2020) 109068.

[9] S. Di Iorio, F. Catapano, A. Magno, P. Sementa, B.M. Vaglieco, Investigation on sub-23 nm particles and their volatile organic fraction (VOF) in PFI/DI spark ignition engine fueled with gasoline, ethanol and a 30% v/v ethanol blend, J. Aerosol Sci. 153 (2021) 105723.

[10] M. Sussman, P. Smereka, S. Osher, A level set approach for computing solutions to incompressible two-phase flow, J. Comput. Phys. 114 (1994) 146–159.

[11] C.W. Hirt, B.D. Nichols, Volume of fluid (VOF) method for the dynamics of free boundaries, J. Comput. Phys. 39 (1981) 201–225.

[12] W. Zhang, J. Wang, S. Yang, B. Li, K. Yu, D. Wang, P. Yongphet, H. Xu, Dynamics of bubble formation on submerged capillaries in a non-uniform direct current electric field, Colloids Surfaces A Physicochem. Eng. Asp. 606 (2020) 125512.

[13] T. Li, S. Wang, S. Li, A.-M. Zhang, Numerical investigation of an underwater explosion bubble based on FVM and VOF, Appl. Ocean Res. 74 (2018) 49–58.

[14] S. Das, L.D. Weerasiri, W. Yang, Influence of surface tension on bubble nucleation, formation and onset of sliding, Colloids Surfaces A Physicochem. Eng. Asp. 516 (2017) 23–31.

[15] M. V Kraposhin, M. Banholzer, M. Pfitzner, I.K. Marchevsky, A hybrid pressure-based solver for nonideal single-phase fluid flows at all speeds, Int. J. Numer. Methods Fluids. 88 (2018) 79–99.

[16] C.H. Yu, H.L. Wen, Z.H. Gu, R.D. An, Numerical simulation of dam-break flow impacting a stationary obstacle by a CLSVOF/IB method, Commun. Nonlinear Sci. Numer. Simul. 79 (2019) 104934.

[17] E. Jafari, M.M. Namin, P. Badiei, Numerical simulation of wave interaction with porous structures, Appl. Ocean Res. 108 (2021) 102522.

[18] F. Garoosi, A.N. Mellado-Cusicahua, M. Shademani, A. Shakibaeinia, Experimental and numerical investigations of dam break flow over dry and wet beds, Int. J. Mech. Sci. 215 (2022) 106946.

[19] C. Yang, W. Cao, Z. Yang, Study on dynamic behavior of water droplet impacting on super-hydrophobic surface with micro-pillar structures by VOF method, Colloids Surfaces A Physicochem. Eng. Asp. 630 (2021) 127634.

[20] Z. Hanene, H. Alla, M. Abdelouahab, T. Roques-Carmes, A numerical model of an immiscible surfactant drop spreading over thin liquid layers using CFD/VOF approach, Colloids Surfaces A Physicochem. Eng. Asp. 600 (2020) 124953.

[21] B.S. de Lima, L. de Souza Meira, F.J. de Souza, Numerical simulation of a water droplet splash: Comparison between PLIC and HRIC schemes for the VoF transport equation, Eur. J. Mech. 84 (2020) 63–70.

[22] S. Yun, Ellipsoidal drop impact on a single-ridge superhydrophobic surface, Int. J. Mech. Sci. 208 (2021) 106677.

[23] R. Ben Kalifa, S. Ben Hamza, N.M. Said, H. Bournot, Fluid flow phenomena in metals processing operations: Numerical description of the fluid flow field by an impinging gas jet on a liquid surface, Int. J. Mech. Sci. 165 (2020) 105220.

[24] R. Kumar, L. Cheng, Y. Xiong, B. Xie, R. Abgrall, F. Xiao, THINC scaling method that bridges VOF and level set schemes, J. Comput. Phys. 436 (2021) 110323.

[25] N. Scapin, P. Costa, L. Brandt, A volume-of-fluid method for interface-resolved simulations of phase-changing two-fluid flows, J. Comput. Phys. 407 (2020) 109251.

[26] G. Tryggvason, B. Bunner, A. Esmaeeli, D. Juric, N. Al-Rawahi, W. Tauber, J. Han, S. Nas, Y.-J. Jan, A front-tracking method for the computations of multiphase flow, J. Comput. Phys. 169 (2001) 708–759.

[27] M. Ishii, T. Hibiki, Thermo-fluid dynamics of two-phase flow, Springer Science & Business Media, 2010.

[28] A. Sharma, Level set method for computational multi-fluid dynamics: A review on developments, applications and analysis, Sadhana. 40 (2015) 627–652.

[29] M. Haghshenas, J.A. Wilson, R. Kumar, Algebraic coupled level set-volume of fluid method for surface tension dominant two-phase flows, Int. J. Multiph. Flow. 90 (2017) 13–28.

[30] K.G. Lyras, B. Hanson, M. Fairweather, P.J. Heggs, A coupled level set and volume of fluid method with a re-initialisation step suitable for unstructured meshes, J. Comput. Phys. 407 (2020) 109224.

[31] Z. Cao, J. Zhou, A. Liu, D. Sun, B. Yu, J. Wei, A three dimensional coupled VOF and Level set (VOSET) method with and without phase change on general curvilinear grids, Chem. Eng. Sci. 223 (2020) 115705.

[32] L. Cui, Z. Chen, Y. Feng, G. Li, J. Liu, An improved VOF method with anti-ventilation techniques for the hydrodynamic assessment of planing hulls-Part 1: Theory, Ocean Eng. (2021) 109687.

[33] I. Malgarinos, N. Nikolopoulos, M. Gavaises, Coupling a local adaptive grid refinement technique with an interface sharpening scheme for the simulation of two-phase flow and free-surface flows using VOF methodology, J. Comput. Phys. 300 (2015) 732–753.

[34] D. Zhang, C. Jiang, D. Liang, L. Cheng, A review on TVD schemes and a refined flux-limiter for steady-state calculations, J. Comput. Phys. 302 (2015) 114–154.

[35] H. Wang, H. Wang, F. Gao, P. Zhou, Z.J. Zhai, Literature review on pressure–velocity decoupling algorithms applied to built-environment CFD simulation, Build. Environ. 143 (2018) 671–678.

[36] J.E. Pilliod Jr, E.G. Puckett, Second-order accurate volume-of-fluid algorithms for tracking material interfaces, J. Comput. Phys. 199 (2004) 465–502.

[37] A. Harten, High resolution schemes for hyperbolic conservation laws, J. Comput. Phys. 135 (1997) 260–278.

[38] F. Kemm, A comparative study of TVD-limiters—well-known limiters and an introduction of new ones, Int. J. Numer. Methods Fluids. 67 (2011) 404–440.

[39] O. Ubbink, R.I. Issa, A method for capturing sharp fluid interfaces on arbitrary meshes, J. Comput. Phys. 153 (1999) 26–50.

[40] F. Garoosi, K. Hooman, Numerical simulation of multiphase flows using an enhanced Volume-of-Fluid (VOF) method, Int. J. Mech. Sci. 215 (2022) 106956.

[41] J.A. Heyns, A.G. Malan, T.M. Harms, O.F. Oxtoby, Development of a compressive surface capturing formulation for modelling free-surface flow by using the volume-of-fluid approach, Int. J. Numer. Methods Fluids. 71 (2013) 788–804.

[42] P. Cifani, W.R. Michalek, G.J.M. Priems, J.G.M. Kuerten, C.W.M. van der Geld, B.J. Geurts, A comparison between the surface compression method and an interface reconstruction method for the VOF approach, Comput. Fluids. 136 (2016) 421–435.

[43] M. Akhlaghi, V. Mohammadi, N.M. Nouri, M. Taherkhani, M. Karimi, Multi-Fluid VoF model assessment to simulate the horizontal air–water intermittent flow, Chem. Eng. Res. Des. 152 (2019) 48–59.

[44] H. Liu, W. Zhang, M. Jia, Y. He, An improved method for coupling the in-nozzle cavitation with Multi-fluid-quasi-VOF model for diesel spray, Comput. Fluids. 177 (2018) 20–32.

[45] S. Kim, N. Oshima, H.J. Park, Y. Murai, Direct numerical simulation of frictional drag modulation in horizontal channel flow subjected to single large-sized bubble injection, Int. J. Multiph. Flow. 145 (2021) 103838.

[46] G. Tretola, K. Vogiatzaki, S. Navarro-Martinez, Implementation of a probabilistic surface density volume of fluid approach for spray atomisation, Comput. Fluids. (2021) 105121.

[47] P. Bruno, G. Di Bella, M. De Marchis, Effect of the contact tank geometry on disinfection efficiency, J. Water Process Eng. 41 (2021) 102035.

[48] H.K. Versteeg, W. Malalasekera, An Introduction To Computational Fluid Dynamics: The Finite Volume Method, Pearson Education, 2007.

[49] R.I. Issa, Solution of the implicitly discretised fluid flow equations by operator-splitting, J. Comput. Phys. 62 (1986) 40–65.

[50] A.J. Chorin, Numerical solution of the Navier-Stokes equations, Math. Comput. 22 (1968) 745–762.

[51] B.J. Parker, D.L. Youngs, Two and three dimensional Eulerian simulation of fluid flow with material interfaces, Atomic Weapons Establishment, 1992.

[52] D.L. Youngs, Time-dependent multi-material flow with large fluid distortion, Numer. Methods Fluid Dyn. 24 (1982) 273–85.

[53] E.G. Puckett, A.S. Almgren, J.B. Bell, D.L. Marcus, W.J. Rider, A high-order projection method for tracking fluid interfaces in variable density incompressible flows, J. Comput. Phys. 130 (1997) 269–282.

[54] A. Nabizadeh, M. Adibifard, H. Hassanzadeh, J. Fahimpour, M.K. Moraveji, Computational fluid dynamics to analyze the effects of initial wetting film and triple contact line on the efficiency of immiscible two-phase flow in a pore doublet model, J. Mol. Liq. 273 (2019) 248–258.

[55] J.U. Brackbill, D.B. Kothe, C. Zemach, A continuum method for modeling surface tension, J. Comput. Phys. 100 (1992) 335–354.

[56] X. Yin, I. Zarikos, N.K. Karadimitriou, A. Raoof, S.M. Hassanizadeh, Direct simulations of two-phase flow experiments of different geometry complexities using Volume-of-Fluid (VOF) method, Chem. Eng. Sci. 195 (2019) 820–827.

[57] Z. Peng, L. Ge, R. Moreno-Atanasio, G. Evans, B. Moghtaderi, E. Doroodchi, VOF-DEM Study of Solid Distribution Characteristics in Slurry Taylor Flow-Based Multiphase Microreactors, Chem. Eng. J. 396 (2020) 124738.

[58] R.F.L. Cerqueira, E.E. Paladino, F. Evrard, F. Denner, B. van Wachem, Multiscale modeling and validation of the flow around Taylor bubbles surrounded with small dispersed bubbles using a coupled VOF-DBM approach, Int. J. Multiph. Flow. 141 (2021) 103673.

[59] Ž. Tuković, M. Perić, H. Jasak, Consistent second-order time-accurate non-iterative PISO-algorithm, Comput. Fluids. 166 (2018) 78–85.

[60] L. Lobovský, E. Botia-Vera, F. Castellana, J. Mas-Soler, A. Souto-Iglesias, Experimental investigation of dynamic pressure loads during dam break, J. Fluids Struct. 48 (2014) 407–434.

[61] C. Zhang, X.Y. Hu, N.A. Adams, A weakly compressible SPH method based on a low-dissipation Riemann solver, J. Comput. Phys. 335 (2017) 605–620.

[62] K. Gong, S. Shao, H. Liu, B. Wang, S.-K. Tan, Two-phase SPH simulation of fluid–structure interactions, J. Fluids Struct. 65 (2016) 155–179.

[63] M. Liu, J. Shao, J. Chang, On the treatment of solid boundary in smoothed particle hydrodynamics, Sci. China Technol. Sci. 55 (2012) 244–254.

[64] A.H. Kashani, A.M. Halabian, K. Asghari, A numerical study of tuned liquid damper based on incompressible SPH method combined with TMD analogy, J. Fluids Struct. 82 (2018) 394–411.

[65] E. Daly, S. Grimaldi, H.H. Bui, Explicit incompressible SPH algorithm for free-surface flow modelling: A comparison with weakly compressible schemes, Adv. Water Resour. 97 (2016) 156–167.

[66] M. Asai, A.M. Aly, Y. Sonoda, Y. Sakai, A stabilized incompressible SPH method by relaxing the density invariance condition, J. Appl. Math. 2012 (2012).

[67] A. Colagrossi, M. Landrini, Numerical simulation of interfacial flows by smoothed particle hydrodynamics, J. Comput. Phys. 191 (2003) 448–475.

[68] F. Garoosi, A. Shakibaeinia, An improved high-order ISPH method for simulation of free-surface flows and convection heat transfer, Powder Technol. 376 (2020) 668–696.

[69] Y. Zhao, H.H. Tan, B. Zhang, A high-resolution characteristics-based implicit dual time-stepping VOF method for free surface flow simulation on unstructured grids, J. Comput. Phys. 183 (2002) 233–273.

[70] N. Grenier, D. Le Touzé, A. Colagrossi, M. Antuono, G. Colicchio, Viscous bubbly flows simulation with an interface SPH model, Ocean Eng. 69 (2013) 88–102.

[71] M. Rezavand, M. Taeibi-Rahni, W. Rauch, An ISPH scheme for numerical simulation of multiphase flows with complex interfaces and high density ratios, Comput. Math. with Appl. 75 (2018) 2658–2677.

[72] Q. Yang, F. Xu, Y. Yang, L. Wang, A multi-phase SPH model based on Riemann solvers for simulation of jet breakup, Eng. Anal. Bound. Elem. 111 (2020) 134–147.

[73] N.J. Quinlan, M. Basa, M. Lastiwka, Truncation error in mesh-free particle methods, Int. J. Numer. Methods Eng. 66 (2006) 2064–2085.

[74] O. Agertz, B. Moore, J. Stadel, D. Potter, F. Miniati, J. Read, L. Mayer, A. Gawryszczak, A. Kravtsov, Å. Nordlund, Fundamental differences between SPH and grid methods, Mon. Not. R. Astron. Soc. 380 (2007) 963–978.

[75] J. Bender, D. Koschier, T. Kugelstadt, M. Weiler, Turbulent micropolar SPH fluids with foam, IEEE Trans. Vis. Comput. Graph. 25 (2018) 2284–2295.

[76] P.N. Sun, A. Colagrossi, S. Marrone, M. Antuono, A.M. Zhang, Multi-resolution Delta-plus-SPH with tensile instability control: Towards high Reynolds number flows, Comput. Phys. Commun. 224 (2018) 63–80.

[77] X. Wen, W. Zhao, D. Wan, A multiphase MPS method for bubbly flows with complex interfaces, Ocean Eng. 238 (2021) 109743.

[78] Y. Xu, G. Yang, Y. Zhu, D. Hu, A coupled SPH–FVM method for simulating incompressible interfacial flows with large density difference, Eng. Anal. Bound. Elem. 128 (2021) 227–243.

[79] I. Farahbakhsh, H.-S. Dou, Derivation of energy gradient function for Rayleigh–Taylor instability, Fluid Dyn. Res. 50 (2018) 45509.

[80] H. Ding, P.D.M. Spelt, C. Shu, Diffuse interface model for incompressible two-phase flows with large density ratios, J. Comput. Phys. 226 (2007) 2078–2095.

[81] Q. Zhang, The motion of a single bubble or spike in Rayleigh-Taylor unstable interfaces, IMPACT Comput. Sci. Eng. 3 (1991) 277–304.

[82] A. Celani, A. Mazzino, P. Muratore-Ginanneschi, L. Vozella, Phase-field model for the Rayleigh–Taylor instability of immiscible fluids, J. Fluid Mech. 622 (2009) 115–134.

[83] J. Glimm, X. Li, A.-D. Lin, Nonuniform approach to terminal velocity for single mode Rayleigh-Taylor instability, Acta Math. Appl. Sin. 18 (2002) 1–8.

[84] M.R. Mankbadi, S. Balachandar, Viscous effects on the non-classical Rayleigh–Taylor instability of spherical material interfaces, Shock Waves. 23 (2013) 603–617.

[85] R. V Morgan, O.A. Likhachev, J.W. Jacobs, Rarefaction-driven Rayleigh–Taylor instability. Part 1. Diffuse-interface linear stability measurements and theory, J. Fluid Mech. 791 (2016) 34–60.

[86] D. Pan, C. Chang, The capturing of free surfaces in incompressible multi-fluid flows, Int. J. Numer. Methods Fluids. 33 (2000) 203–222.

[87] F. Garoosi, T. Merabtene, T.-F. Mahdi, Numerical simulation of merging of two rising bubbles with different densities and diameters using an enhanced Volume-Of-Fluid (VOF) model, Ocean Eng. 247 (2022) 110711.

[88] H.Y. Li, Y.F. Yap, J. Lou, Z. Shang, Numerical modelling of three-fluid flow using the level-set method, Chem. Eng. Sci. 126 (2015) 224–236.

[89] Z. Jávor, N. Schreithofer, K. Heiskanen, The effect of bubble release techniques on their behaviour at the initial stages of rise, Miner. Eng. 36 (2012) 254–261.

[90] J. Zawala, D. Kosior, K. Malysa, Formation and influence of the dynamic adsorption layer on kinetics of the rising bubble collisions with solution/gas and solution/solid interfaces, Adv. Colloid Interface Sci. 222 (2015) 765–778.

[91] K. Malysa, M. Krasowska, M. Krzan, Influence of surface active substances on bubble motion and collision with various interfaces, Adv. Colloid Interface Sci. 114 (2005) 205–225.

[92] G. Kong, H. Mirsandi, K.A. Buist, E. Peters, M.W. Baltussen, J.A.M. Kuipers, Oscillation dynamics of a bubble rising in viscous liquid, Exp. Fluids. 60 (2019) 1–13.

[93] S.L. Manzello, J.C. Yang, An experimental study of a water droplet impinging on a liquid

surface, Exp. Fluids. 32 (2002) 580–589.

[94] Y. Shang, Y. Zhang, Y. Hou, B. Bai, X. Zhong, Effects of surface subcooling on the spreading dynamics of an impact water droplet, Phys. Fluids. 32 (2020) 123309.

[95] J.H. Yang, C.Y. Lee, Experimental study on phenomena of single water droplet impacts on liquid surfaces: Pattern maps and correlations, Exp. Therm. Fluid Sci. 130 (2022) 110480.

[96] M. Kumar, R. Bhardwaj, K.C. Sahu, Coalescence dynamics of a droplet on a sessile droplet, Phys. Fluids. 32 (2020) 12104.

[97] M. Taghilou, M.H. Rahimian, Lattice Boltzmann model for thermal behavior of a droplet on the solid surface, Int. J. Therm. Sci. 86 (2014) 1–11.

[98] H.-Y. Kim, J.-H. Chun, The recoiling of liquid droplets upon collision with solid surfaces, Phys. Fluids. 13 (2001) 643–659.

[99] X. Gao, R. Li, Spread and recoiling of liquid droplets impacting solid surfaces, AIChE J. 60 (2014) 2683–2691.

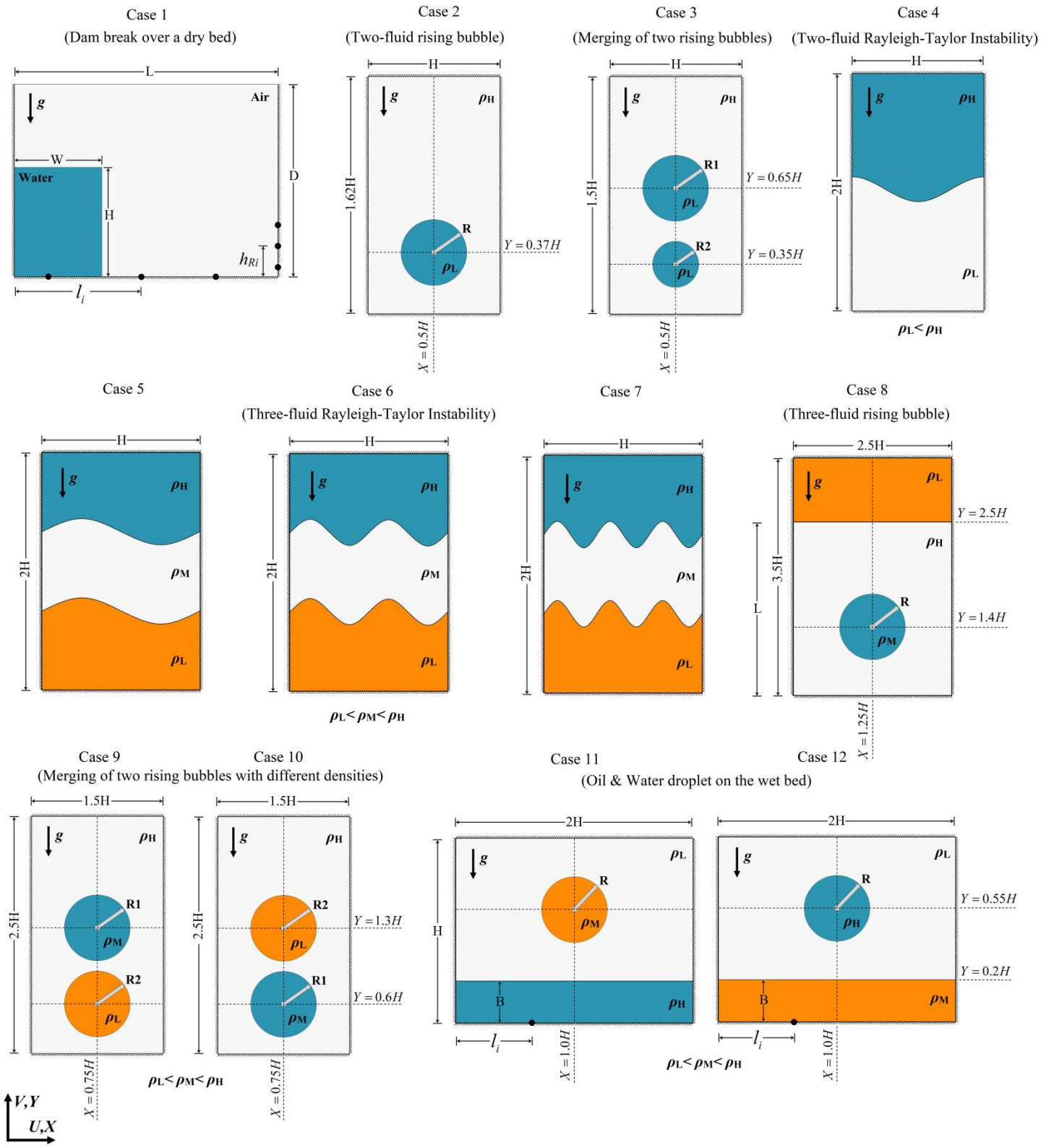

Fig.1. Schematic diagram of different physical configurations under consideration with associated boundary conditions and coordinate system.

(a) Contours of volume fraction field (b) Contours of pressure field

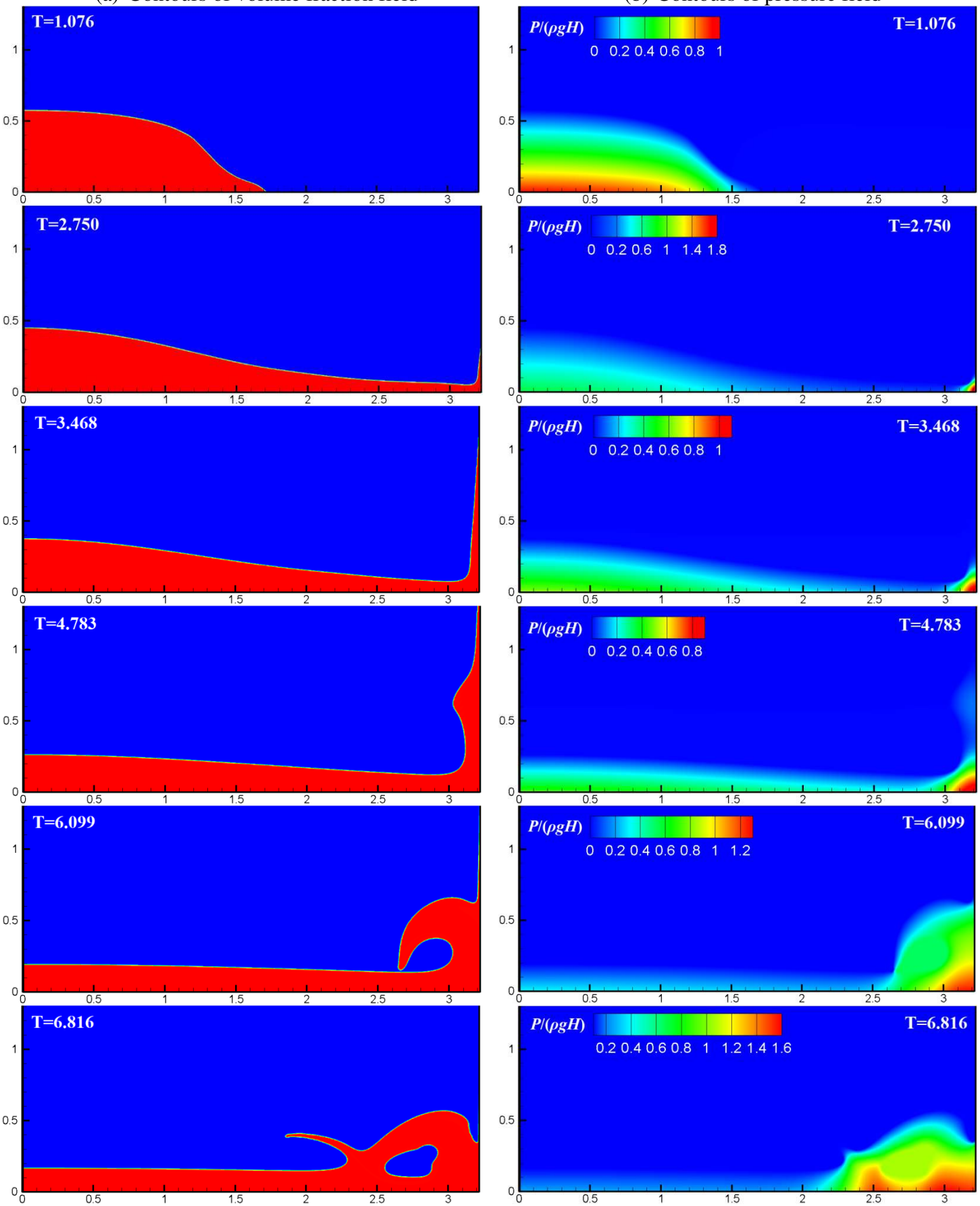

Fig. 2. Time evolution of dam-break flow (case 1) in forms of the volume-fraction and pressure fields calculated in the current study at different time instants.

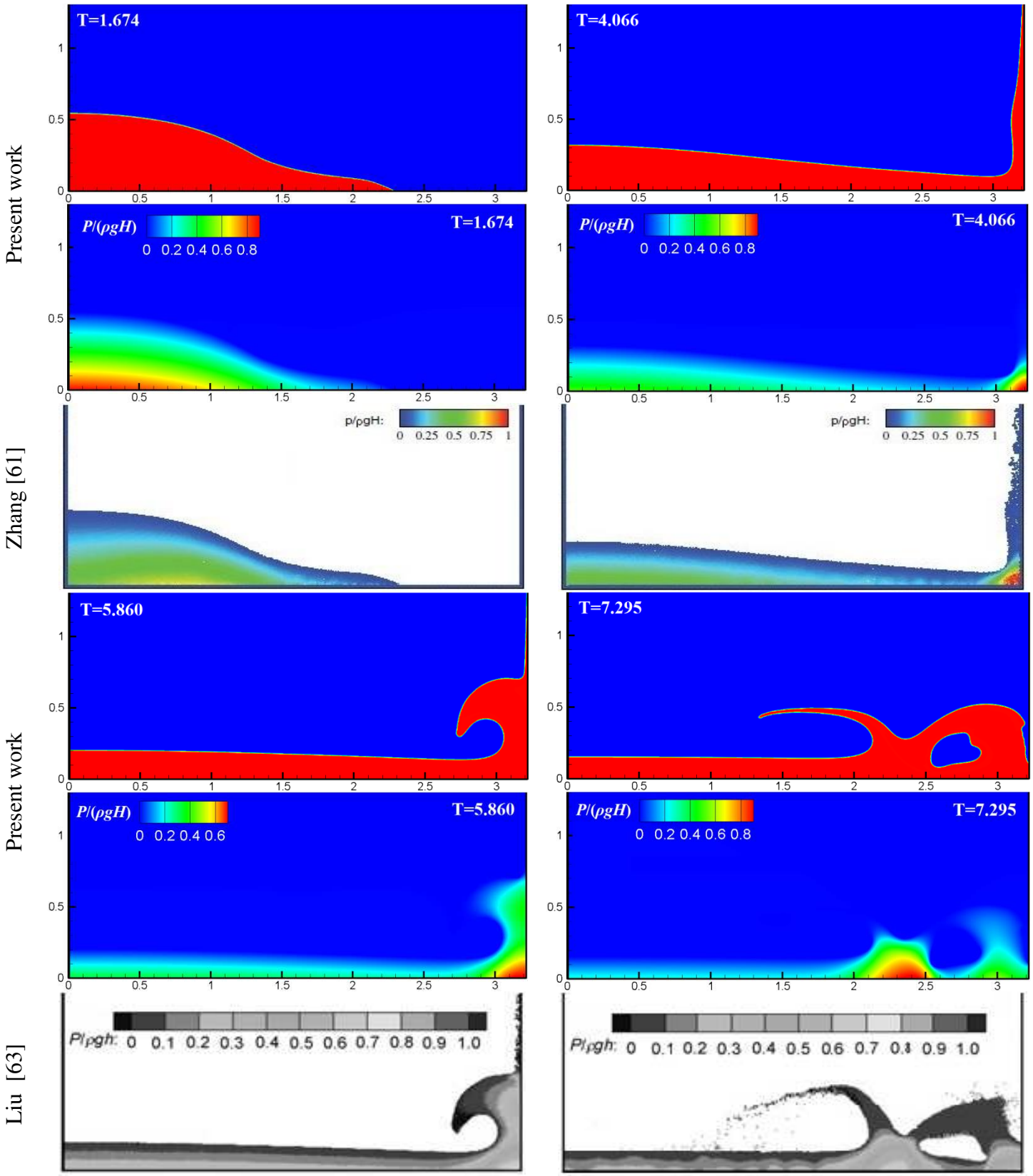

Fig. 3. Qualitative comparisons of the calculated results in forms of pressure and volume fraction field from the current work with numerical results of Liu et al. [63] and Zhang et al. [61] at different time instants for case 1.

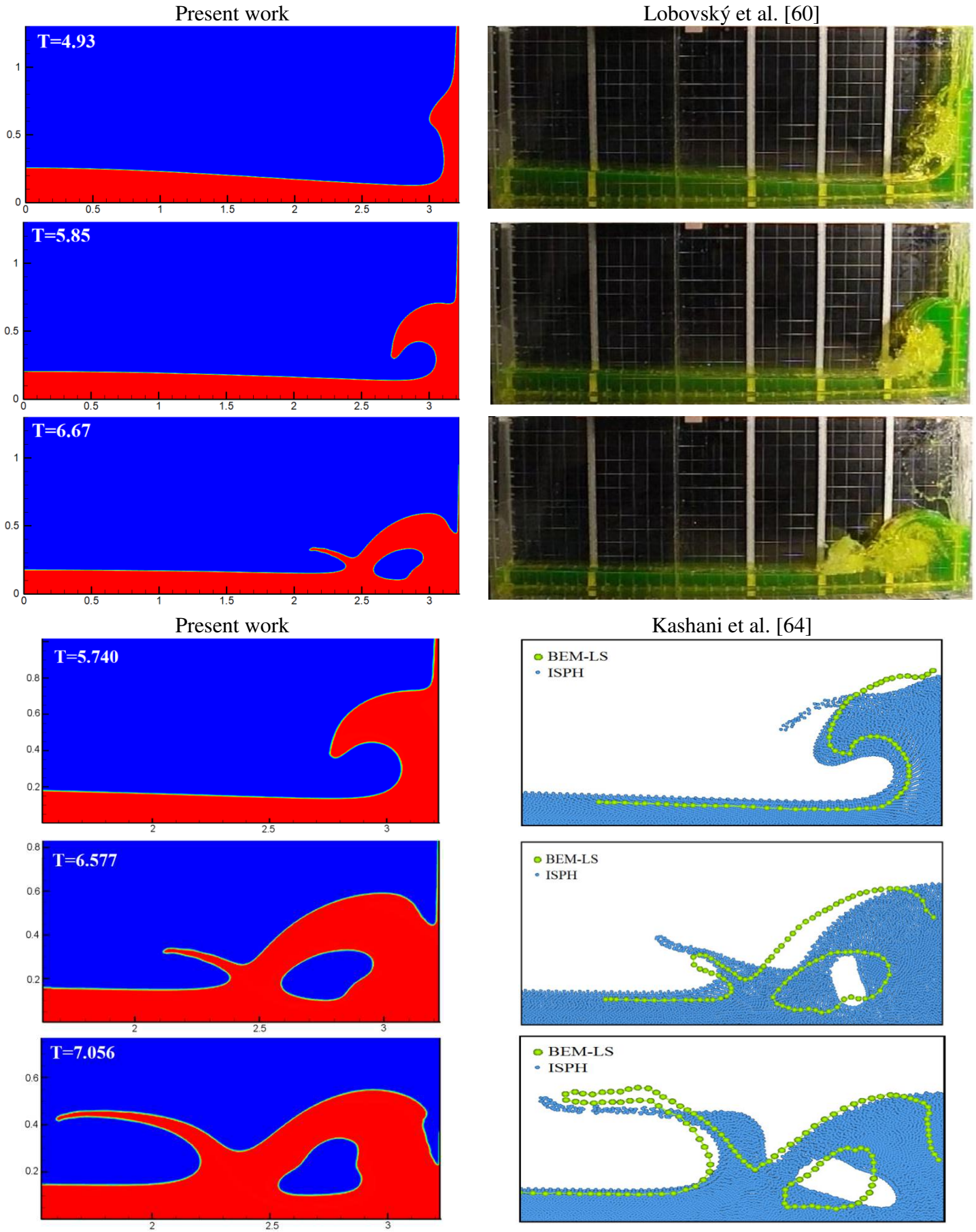

Fig. 4. Qualitative comparisons of the calculated results from the current work with numerical and experimental results of Kashani et al. [64] and Lobovský et al. [60] at different time instants for case 1.

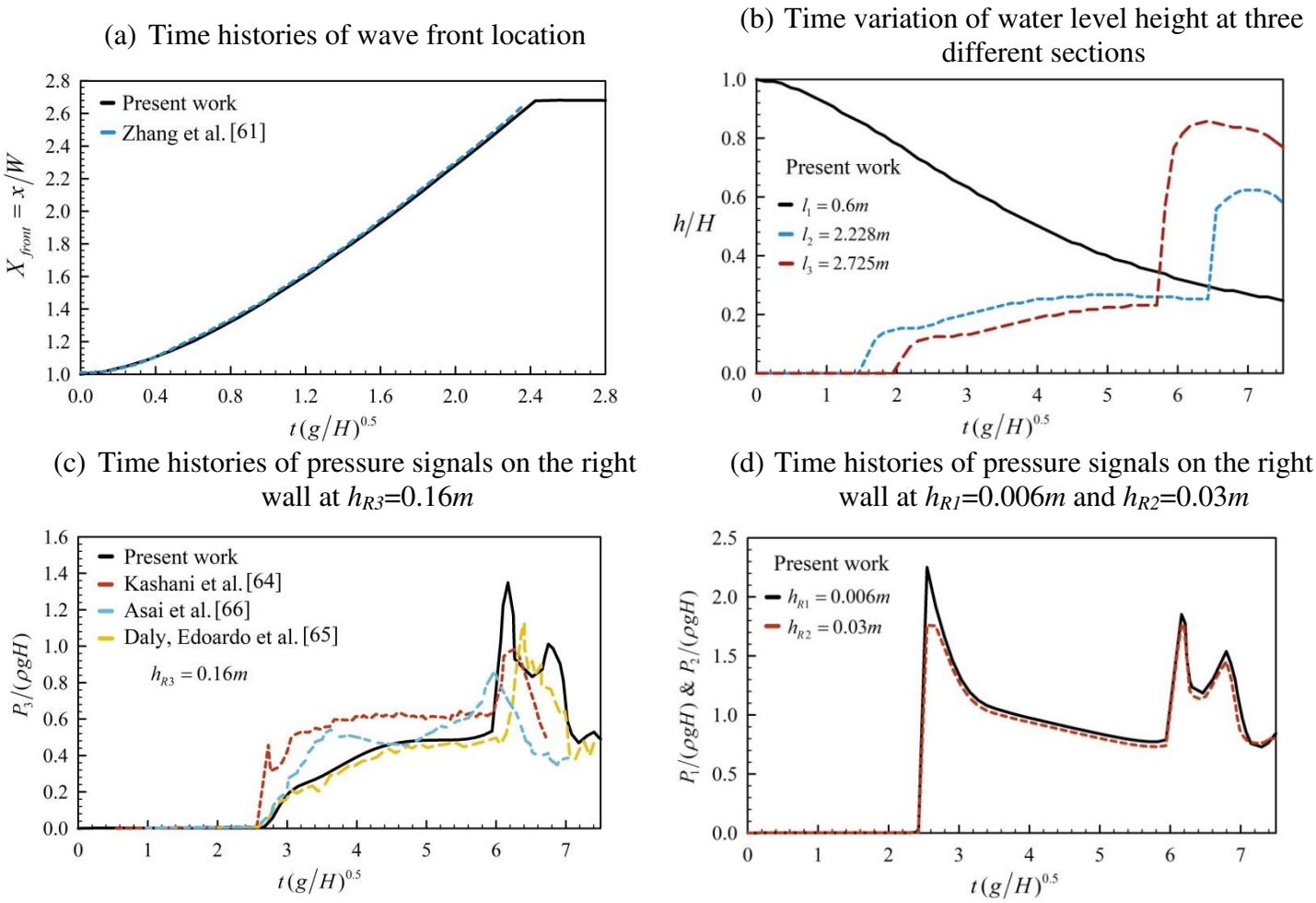

Fig. 5. Qualitative and quantitative comparison of the calculated results with numerical results of Kashani et al. [64], Zhang et al. [61], Daly-Edoardo et al [65] and Asai et al [66] for case 1.

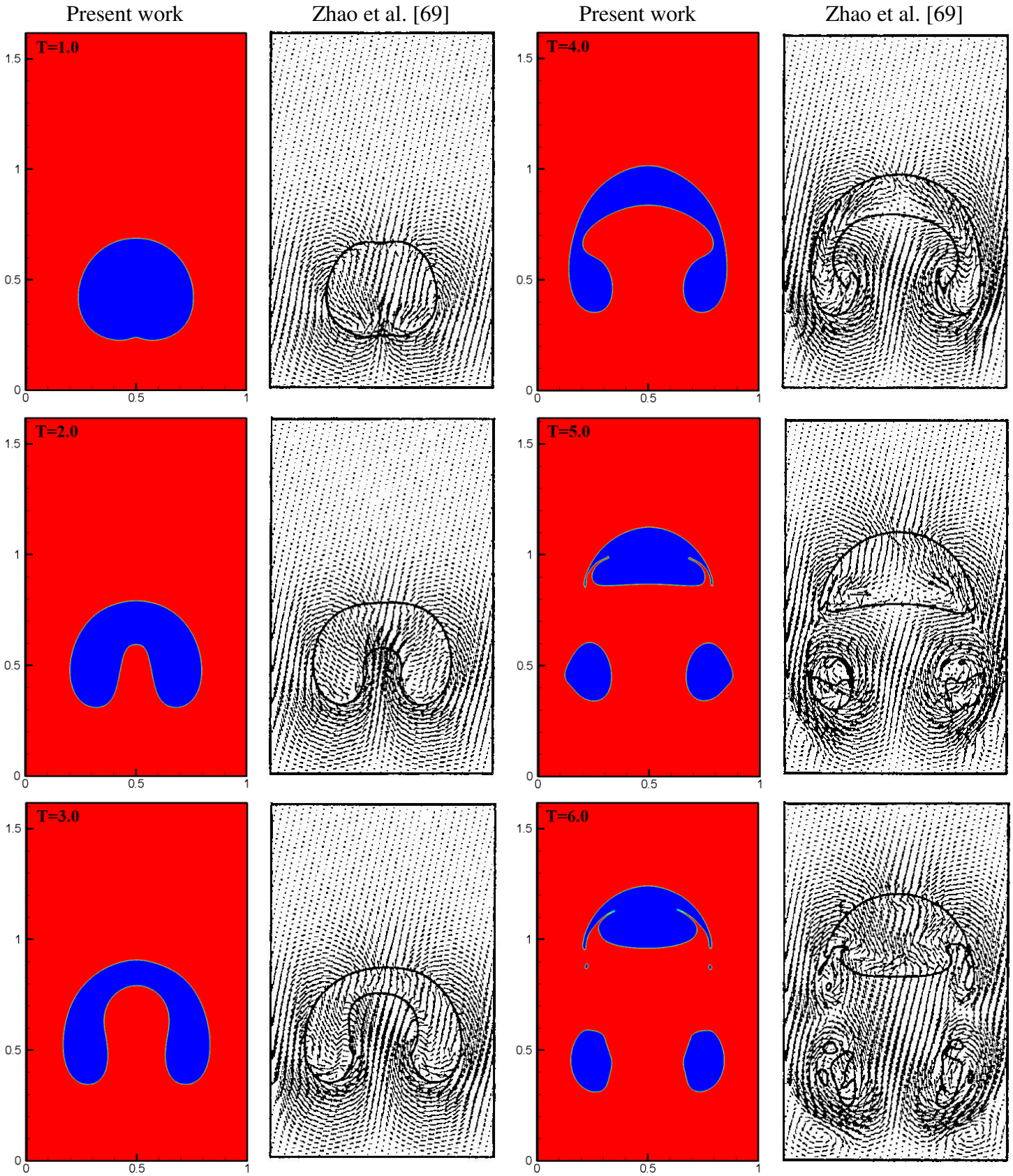

Fig. 6. Qualitative comparisons of the calculated results in term of volume fraction field from the current work with numerical results of Zhao et al. [69] at different time instants for the case of single bubble rising (case 2).

(a) Zoomed in view of the daughter bubble at T=6.0

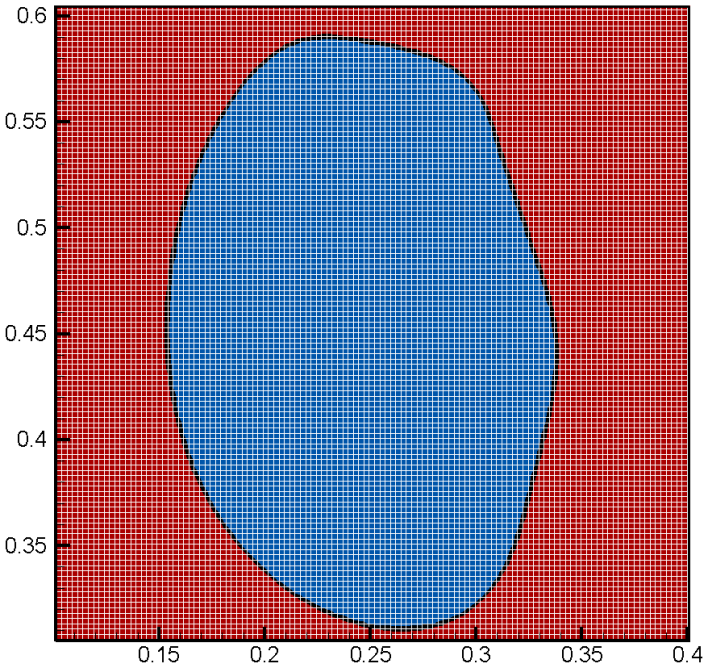

(b) Time history of bubble front position

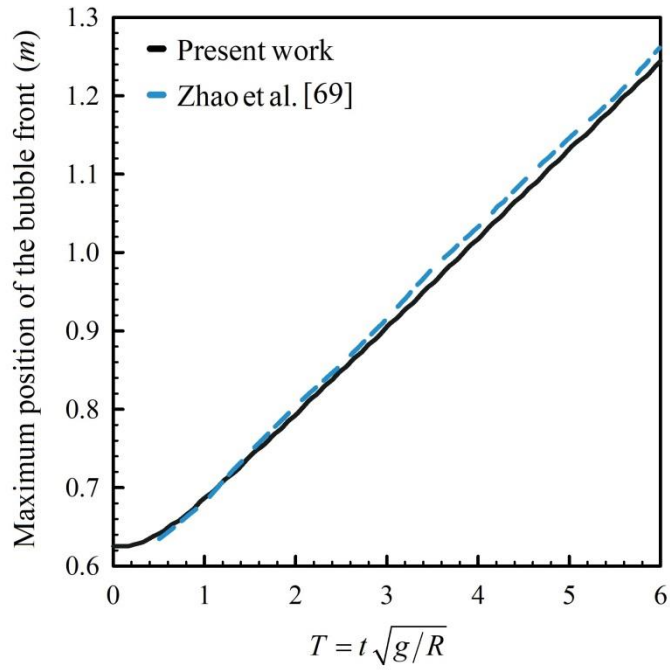

Fig. 7. Quantitative comparison of the calculated results with numerical results of Zhao et al. [69] for case 2.

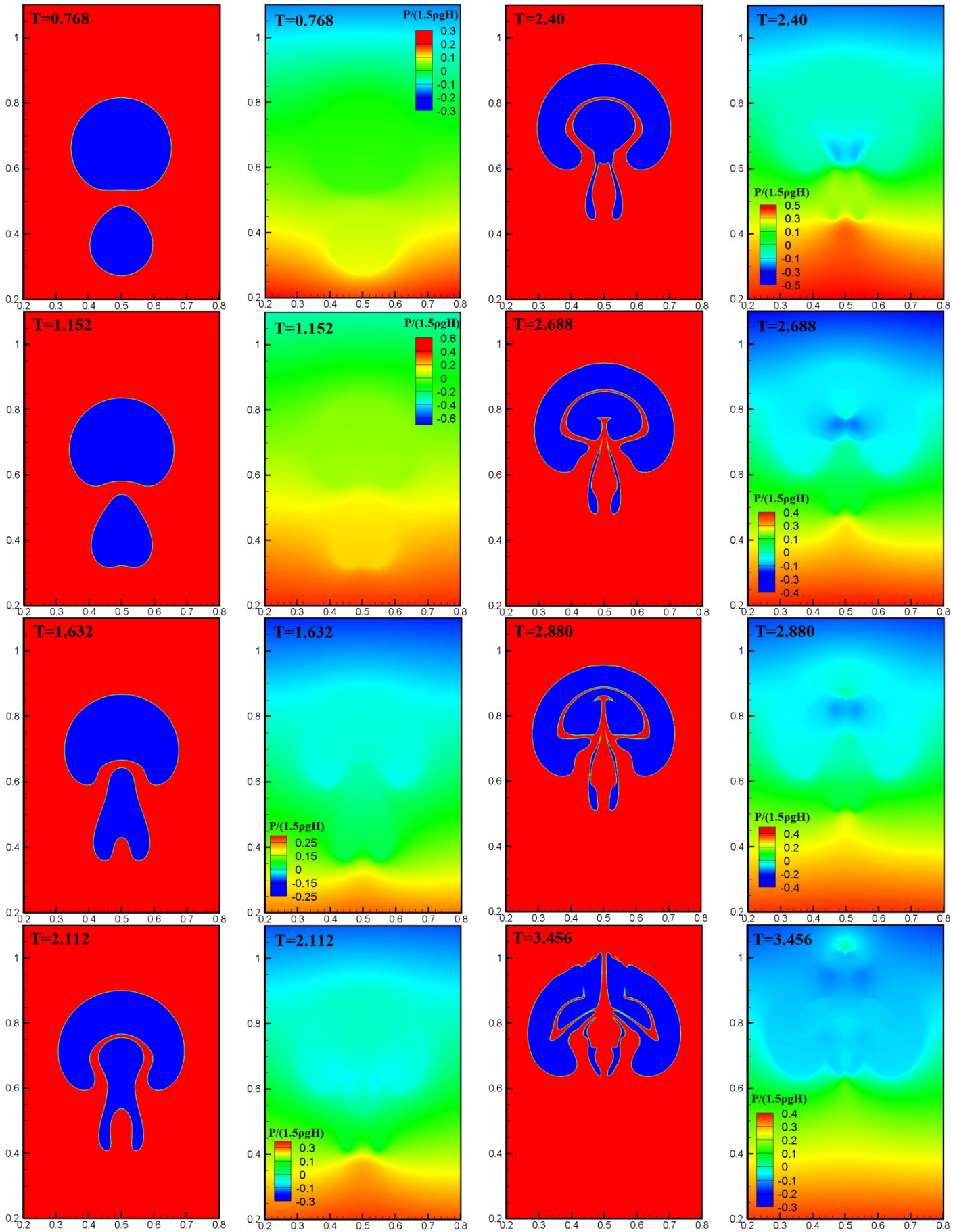

Fig. 8. Time evolution of merging of two rising bubbles (case 3) in forms of the volume-fraction and pressure fields calculated in the present work at different time instants.

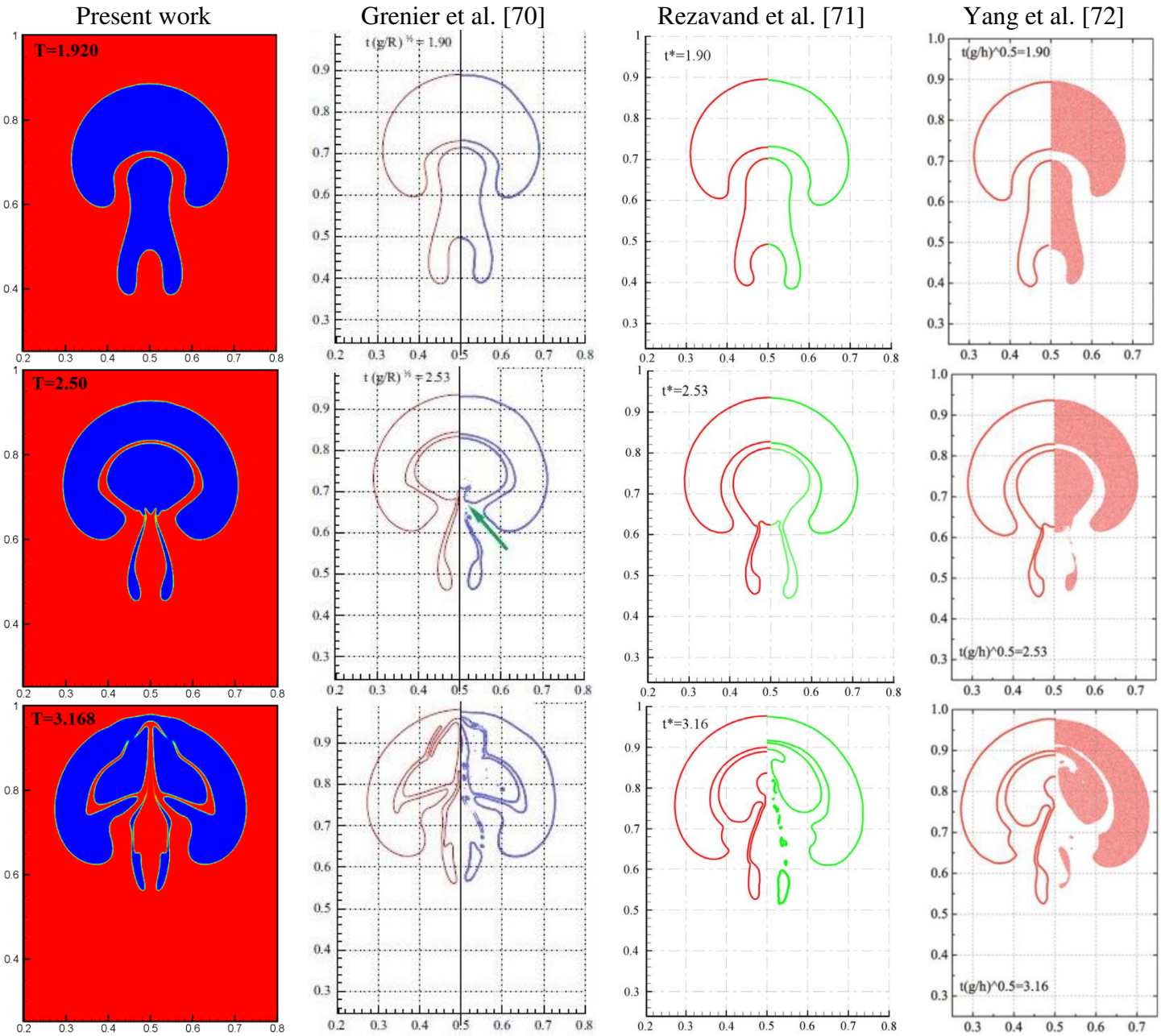

Fig. 9. Qualitative comparisons of the calculated results from the current work with numerical results of Grenier et al. [70], Rezavand et al. [71] and Yang et al. [72] at different time instants for case 3.

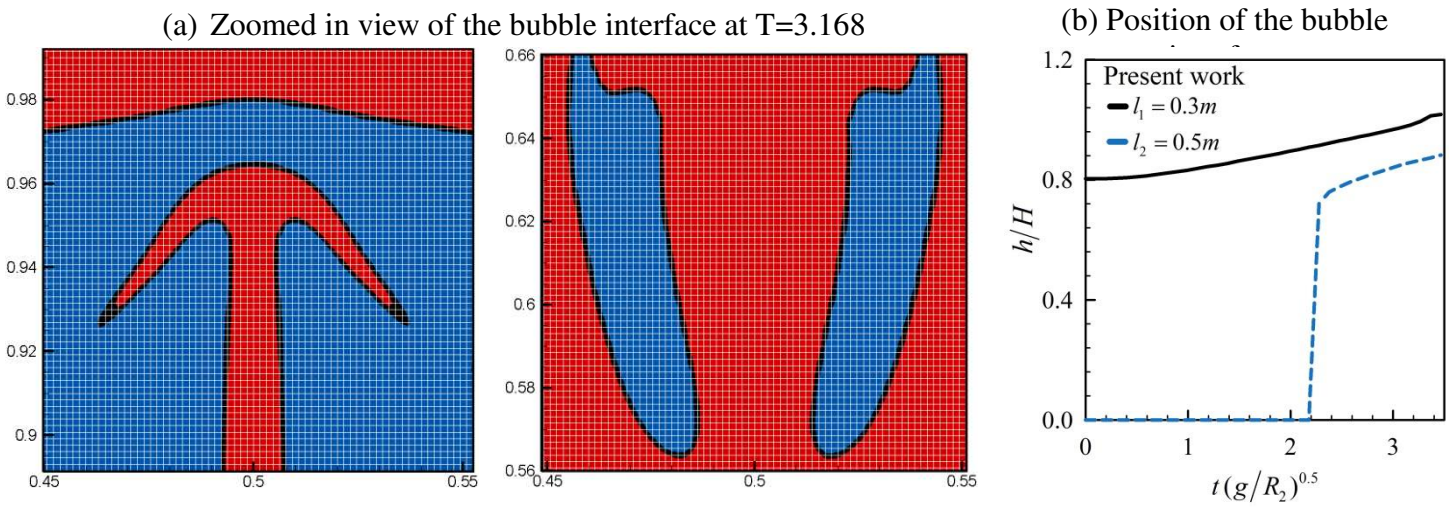

Fig. 10. (a) Zoomed in view of the bubble interface at T=3.168 and time history of maximum position of the bubble interface calculated from the current work at two different sections in case 3, l_1=0.3m and l_2=0.5m.

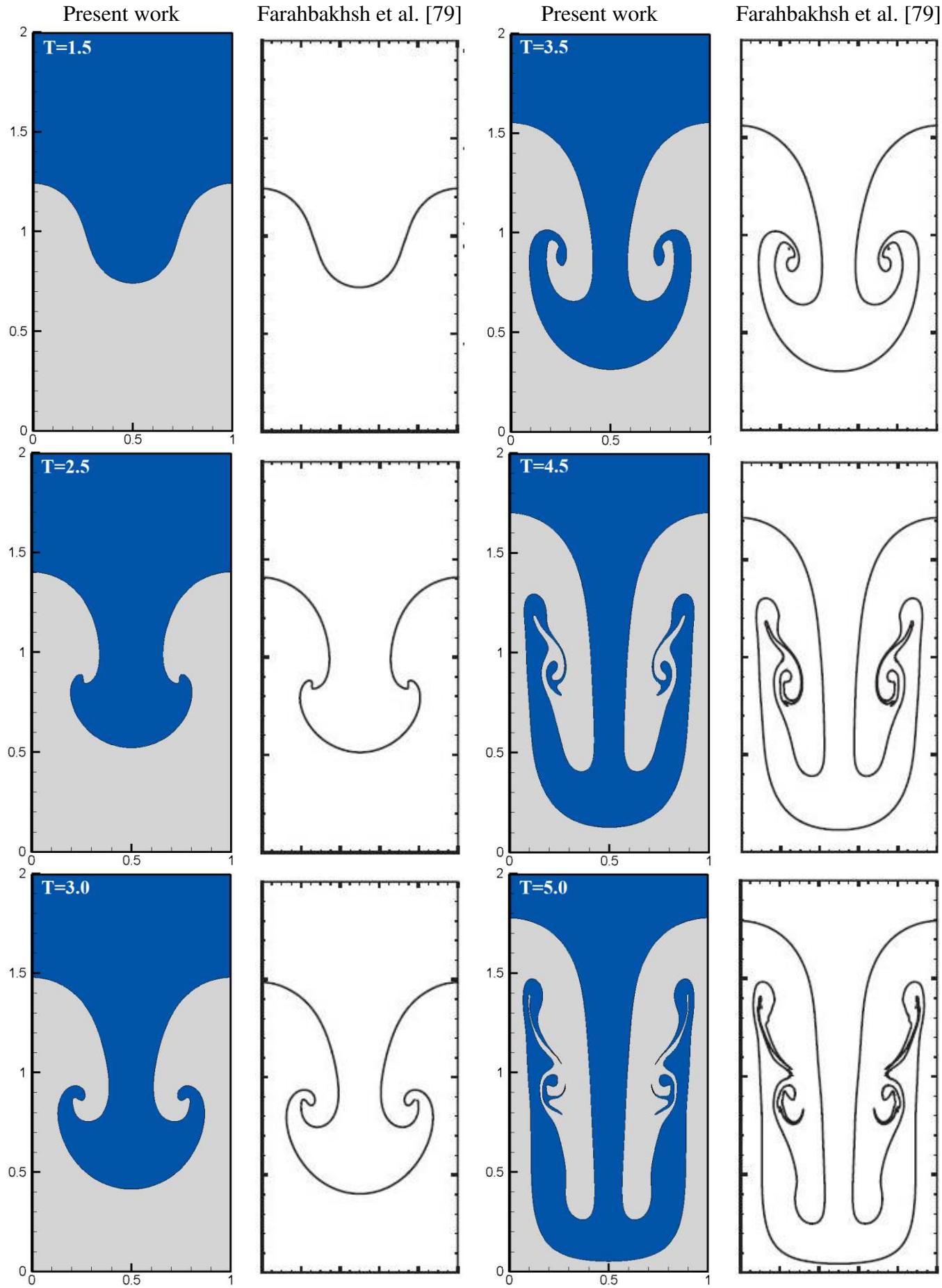

Fig. 11. Qualitative comparison of the obtained results with numerical data of Farahbakhsh et al. [79] in case 4.

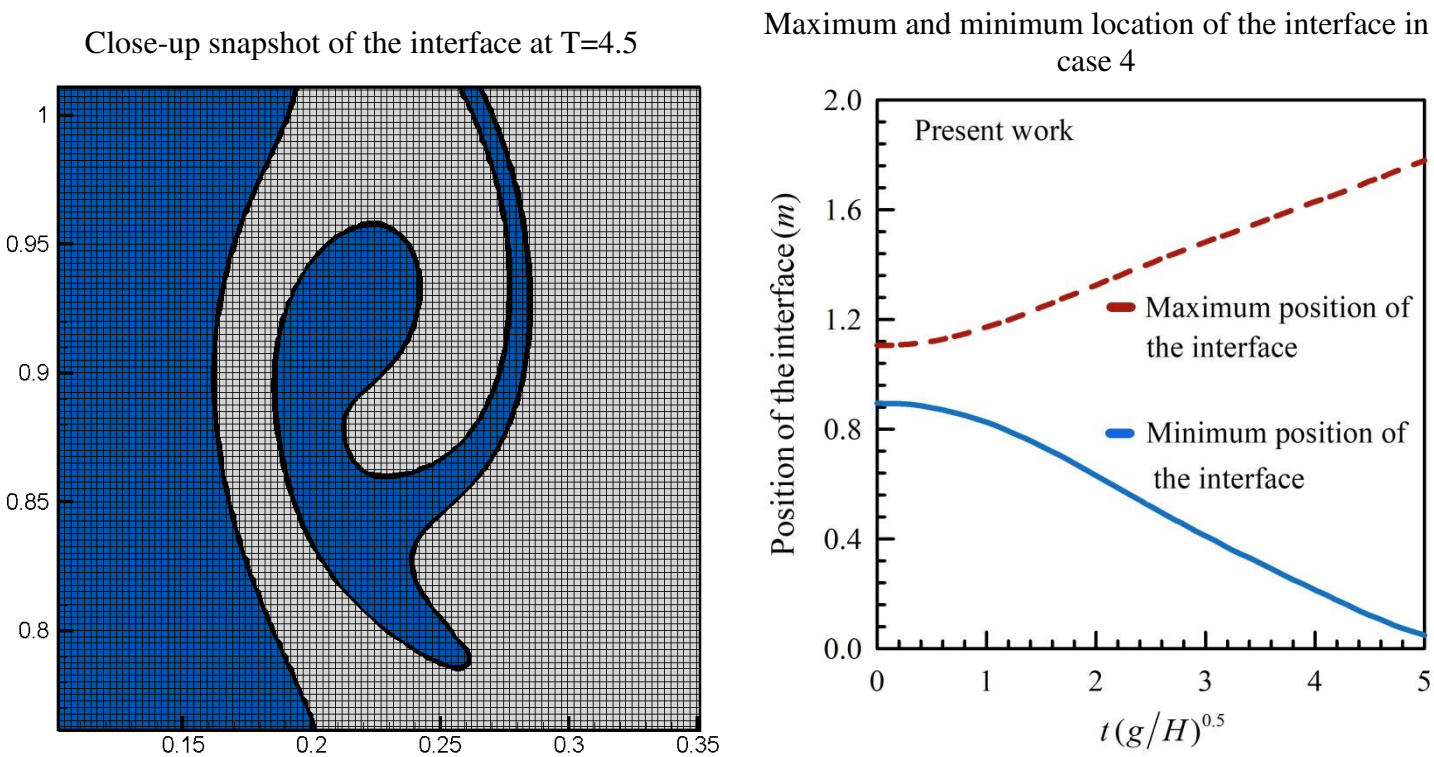

Fig. 12. Close-up snapshot of the interface at T=4.5 and maximum and minimum position of the interface calculated from the present study for case 4 (Two-phase Rayleigh-Taylor Instability)

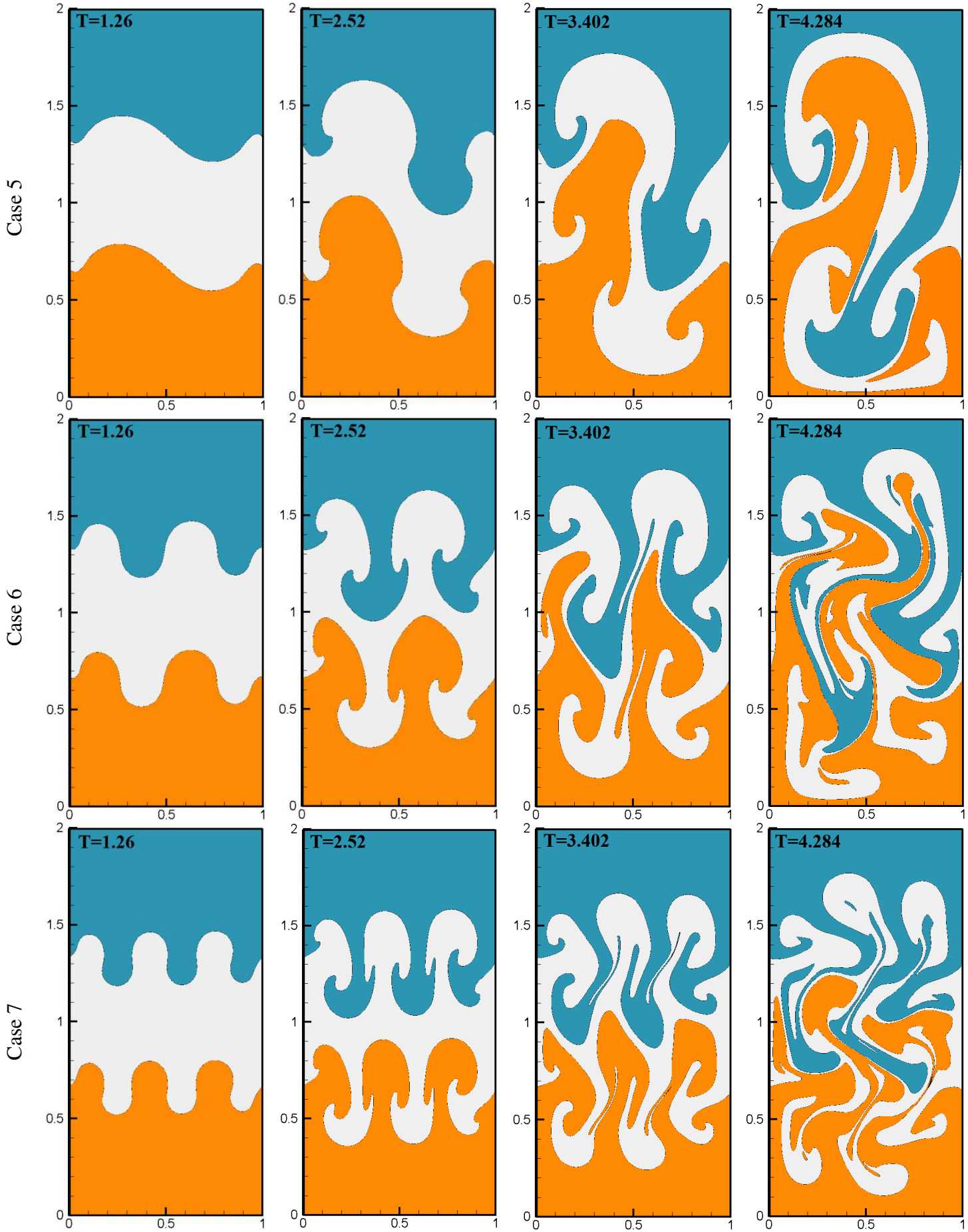

Fig. 13. Time evolution of three-fluid Rayleigh-Taylor Instability in cases 5, 6 and 7 at different time instants.

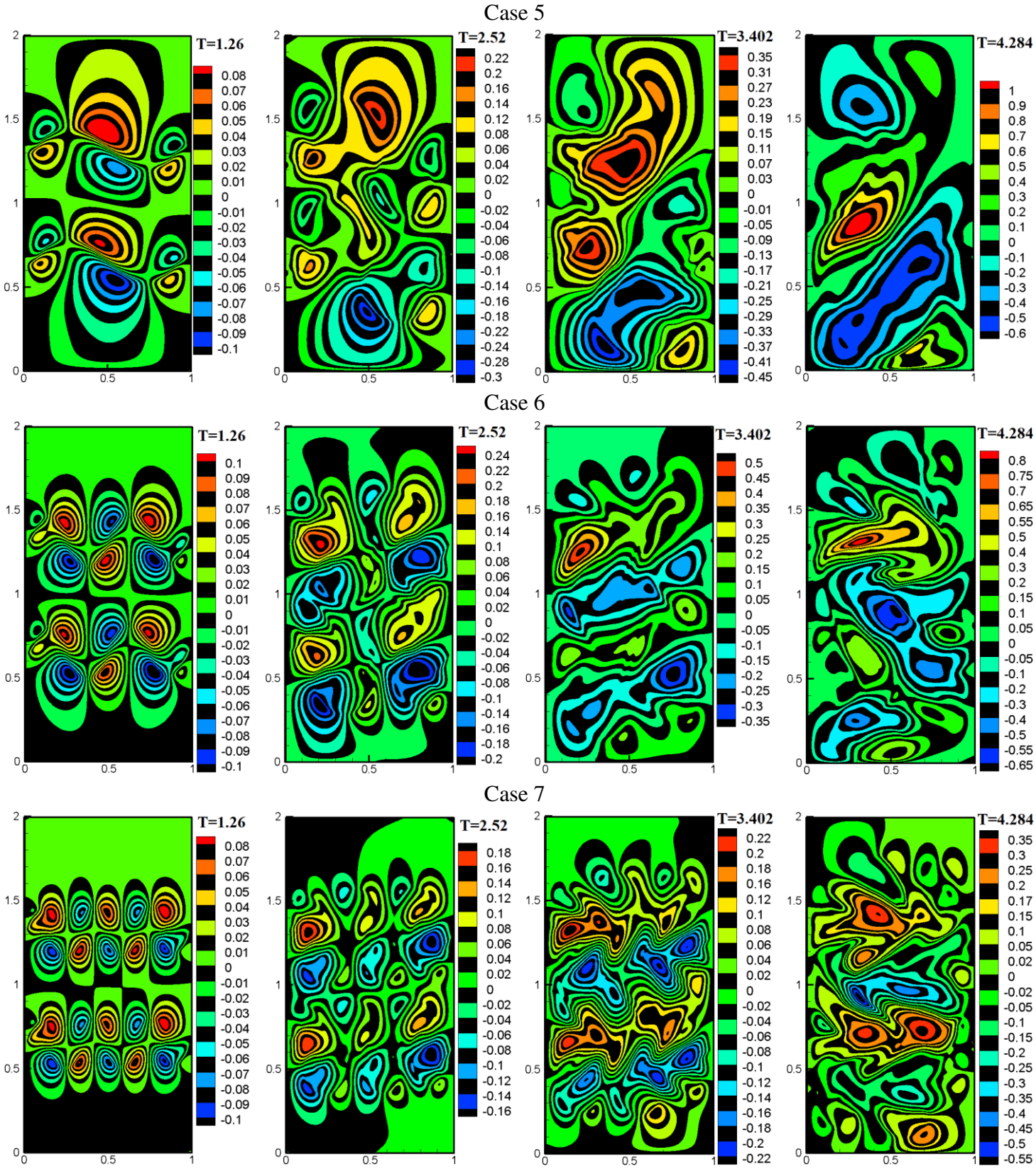

Fig. 14. Contours of non-dimensional velocity in the x-directions (U) in cases 5, 6 and 7 at different non-dimensional time instants ($T = t\sqrt{g/H}$).

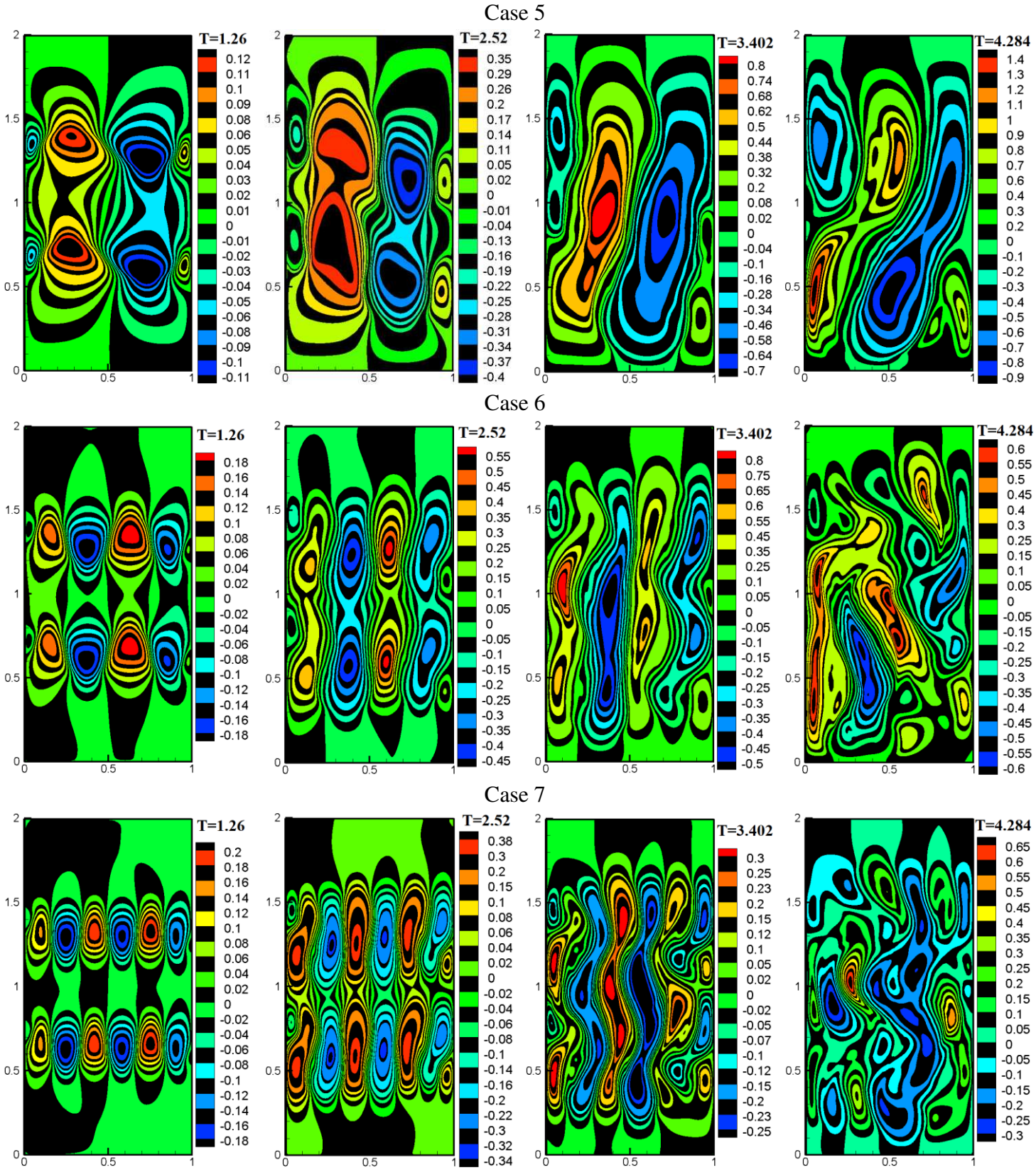

Fig. 15. Contours of non-dimensional velocity in the *y*-directions (*V*) in cases 5, 6 and 7 at different non-dimensional time instants ($T = t\sqrt{g/H}$).

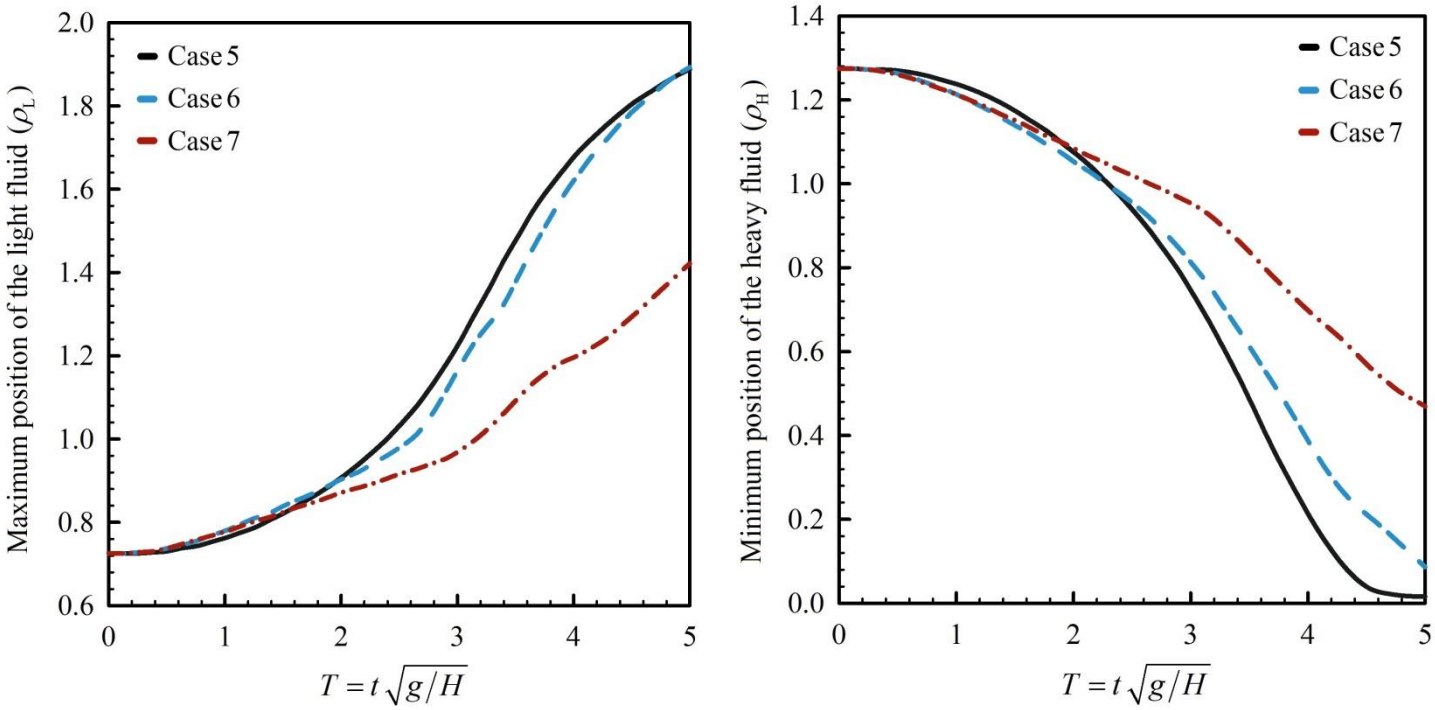

Fig. 16. Time variation of maximum and minimum positions of the light and dense fluids in cases 5, 6 and 7 (three-fluid Rayleigh-Taylor Instability problems).

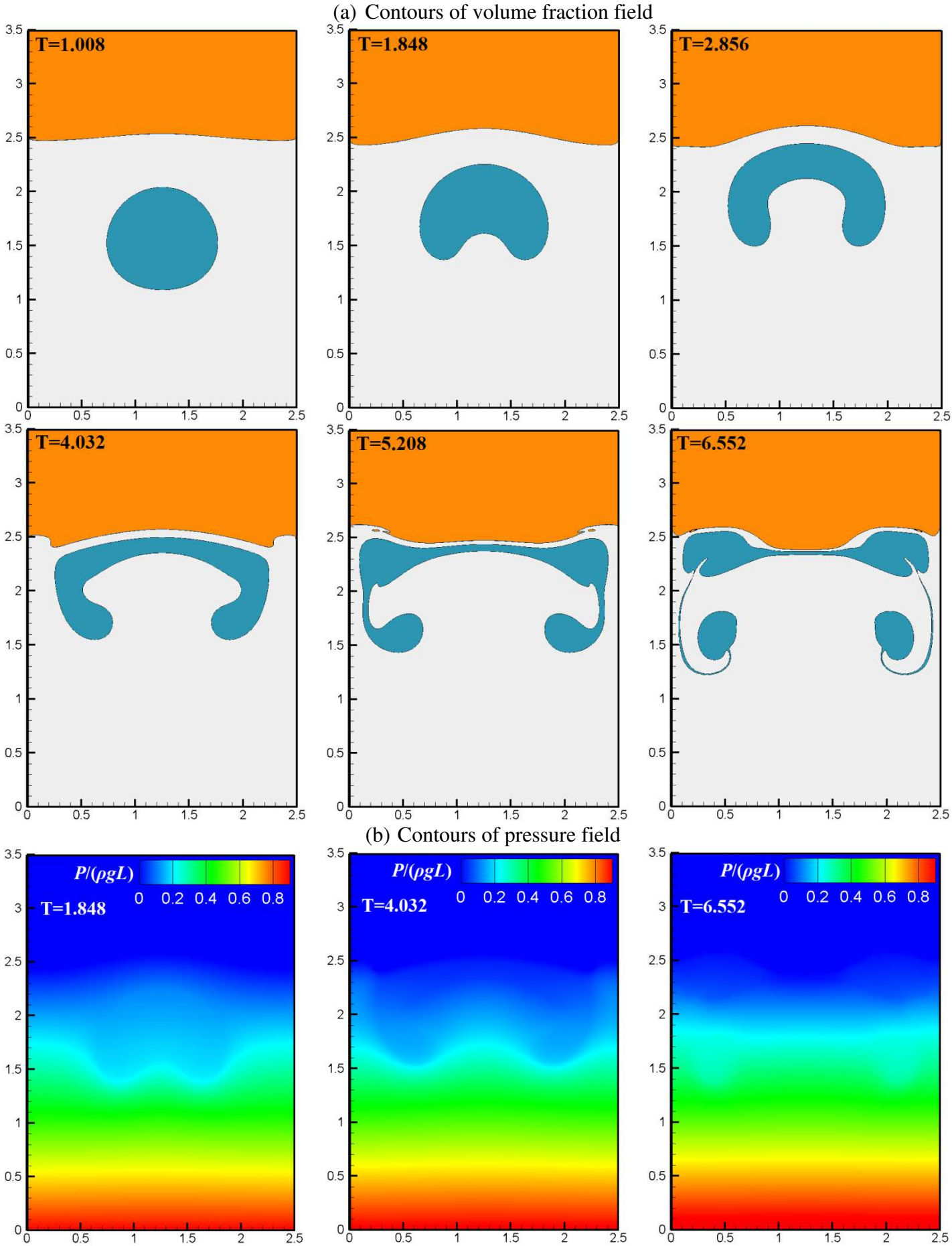

Fig. 17. Time evolution of three-fluid rising bubble (case 8) at different time instants ($T = t\sqrt{g/(2R)}$).

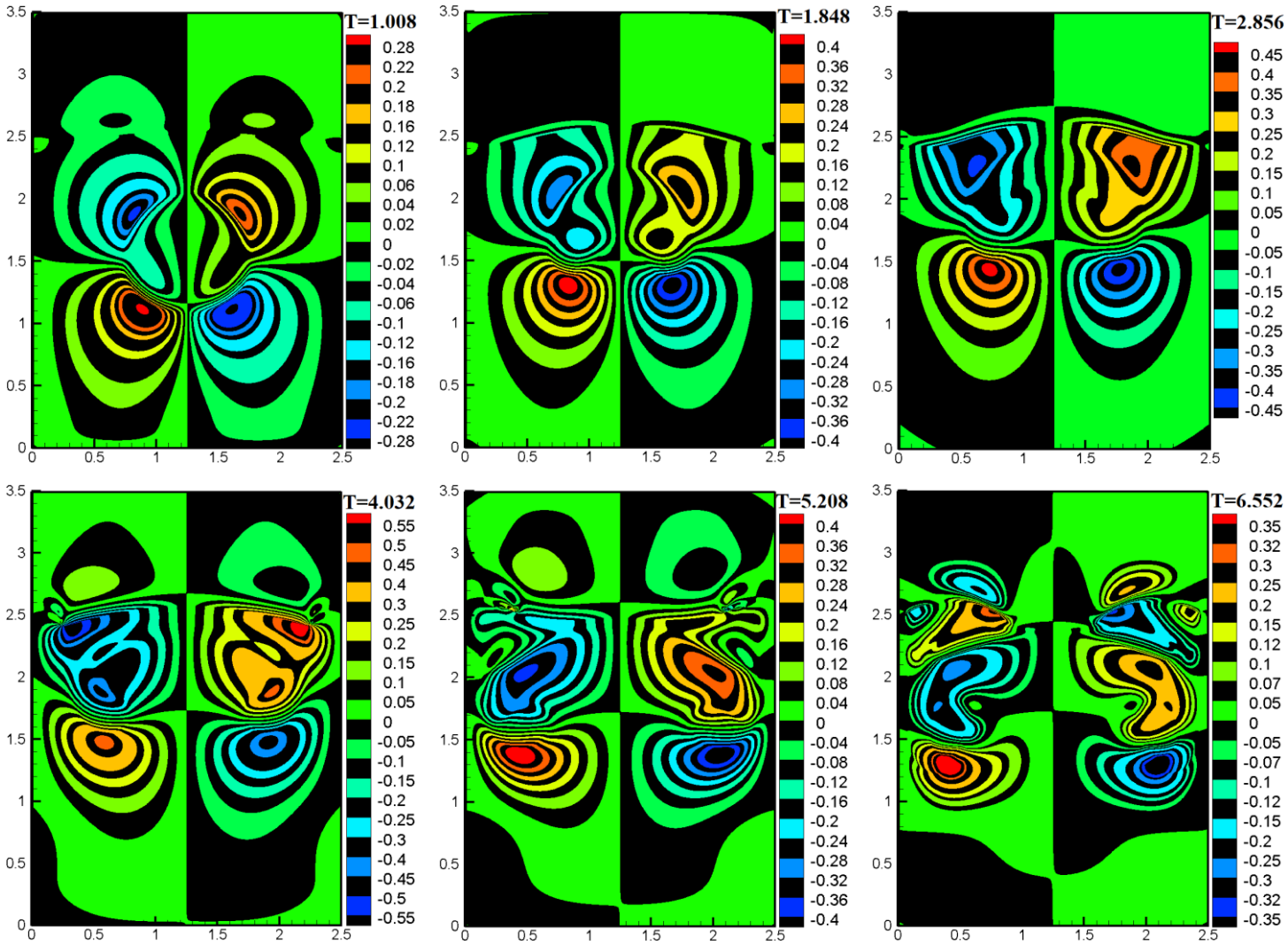

Fig. 18. Contours of non-dimensional velocity in the x-directions (U) in case 8 (three-fluid rising bubble) at different non-dimensional time instants ($T = t\sqrt{g/(2R)}$).

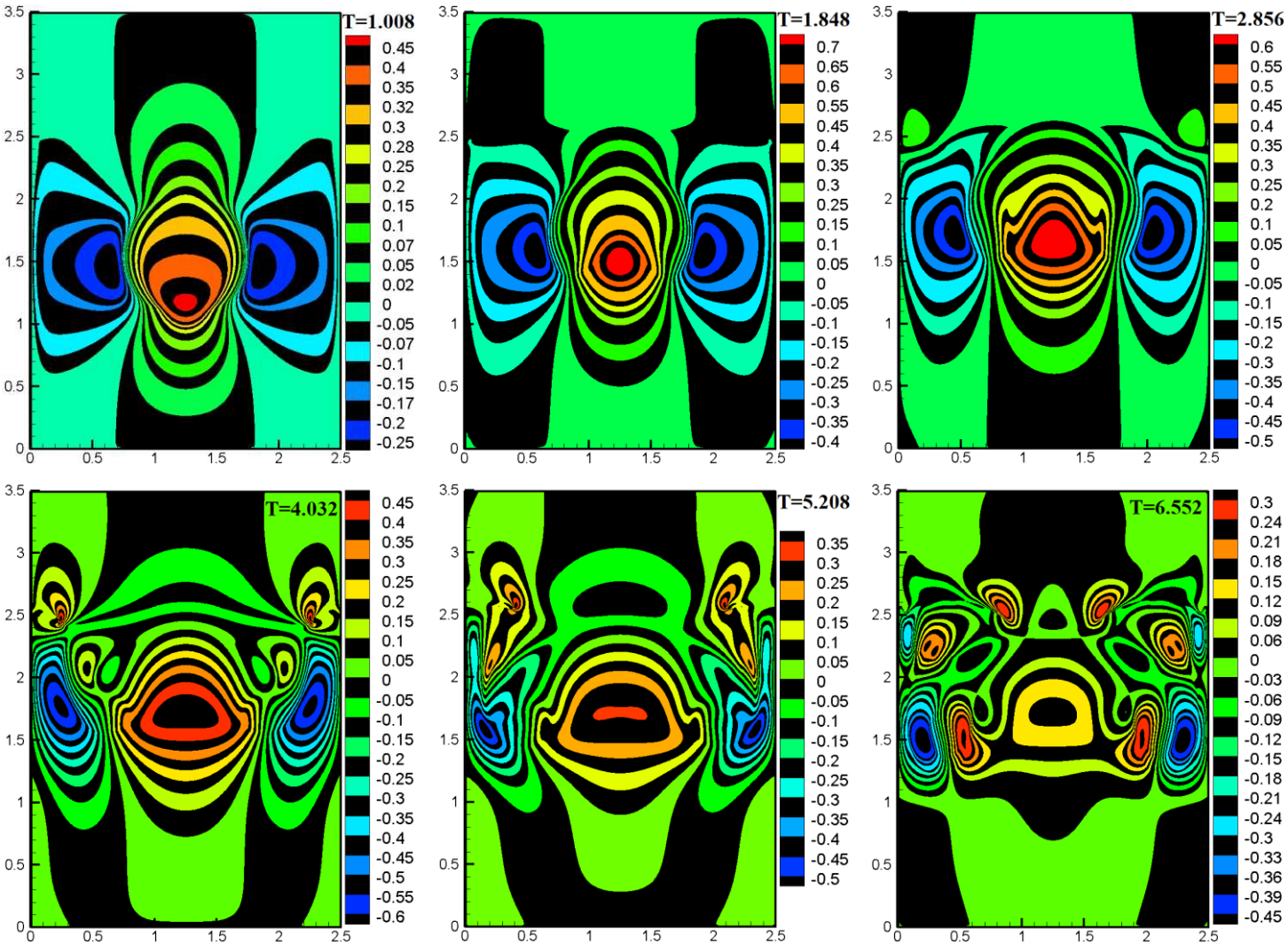

Fig. 19. Contours of non-dimensional velocity in the *y*-directions (*V*) in case 8 (three-fluid rising bubble) at different non-dimensional time instants ($T = t\sqrt{g/(2R)}$).

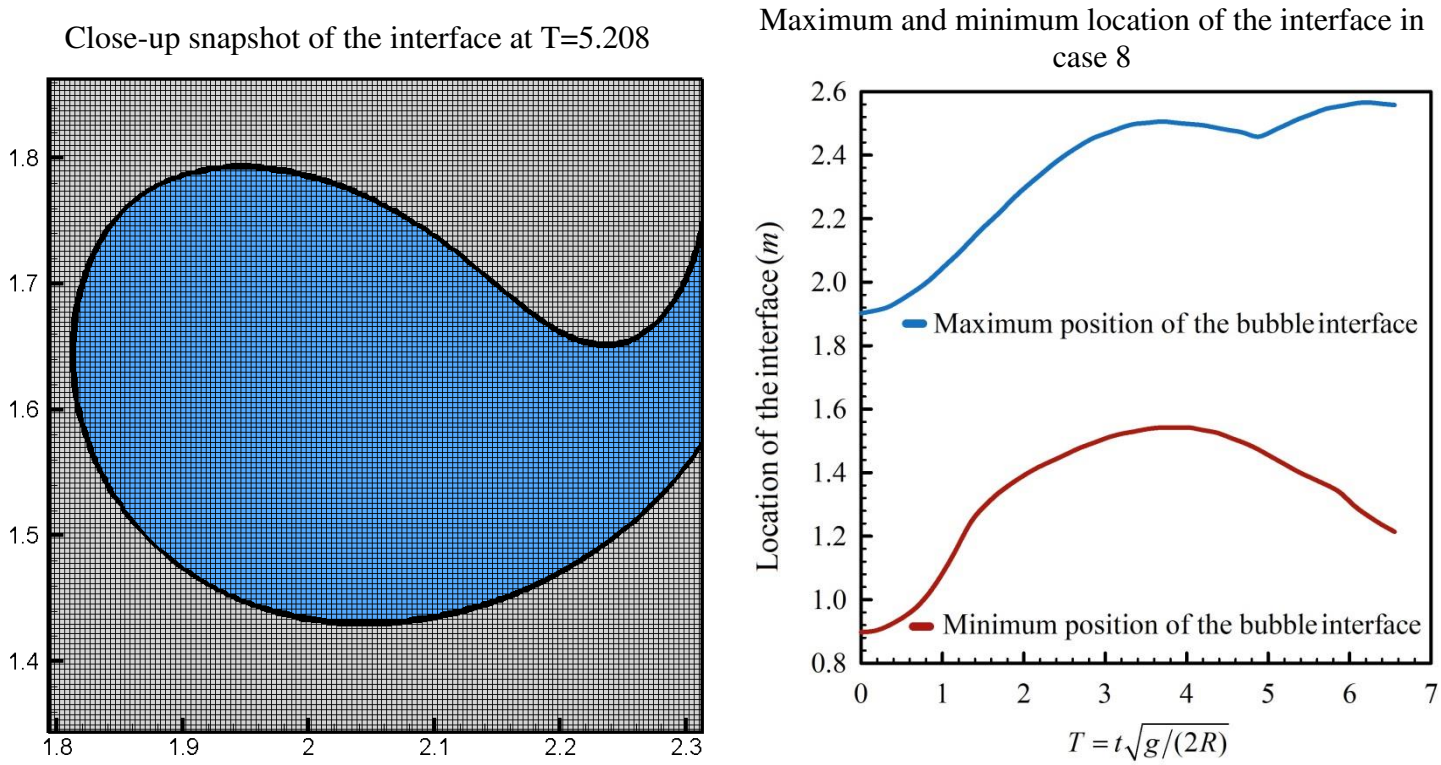

Fig. 20. Close-up snapshot of the bubble interface at T=5.208 and maximum and minimum position of the bubble interface calculated from the present work in case 8 (three-fluid rising bubble).

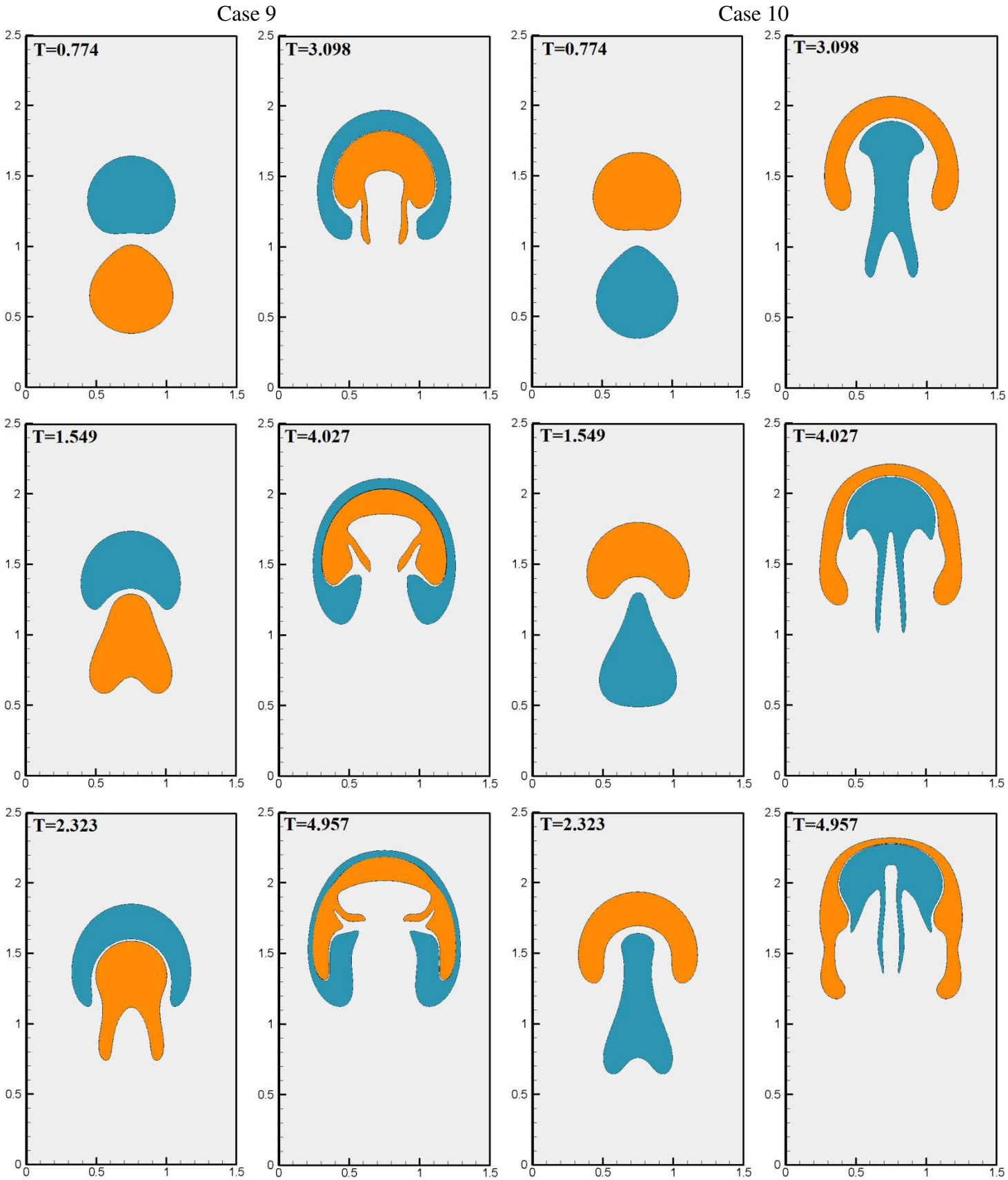

Fig. 21. Transient evolutions of merging of two rising bubbles with different densities in forms of the volume-fraction field calculated from the current work at different time instants ($T = t\sqrt{g/(2R_1)}$). Cases 9 and 10. $R_1 = R_2 = 0.3m$.

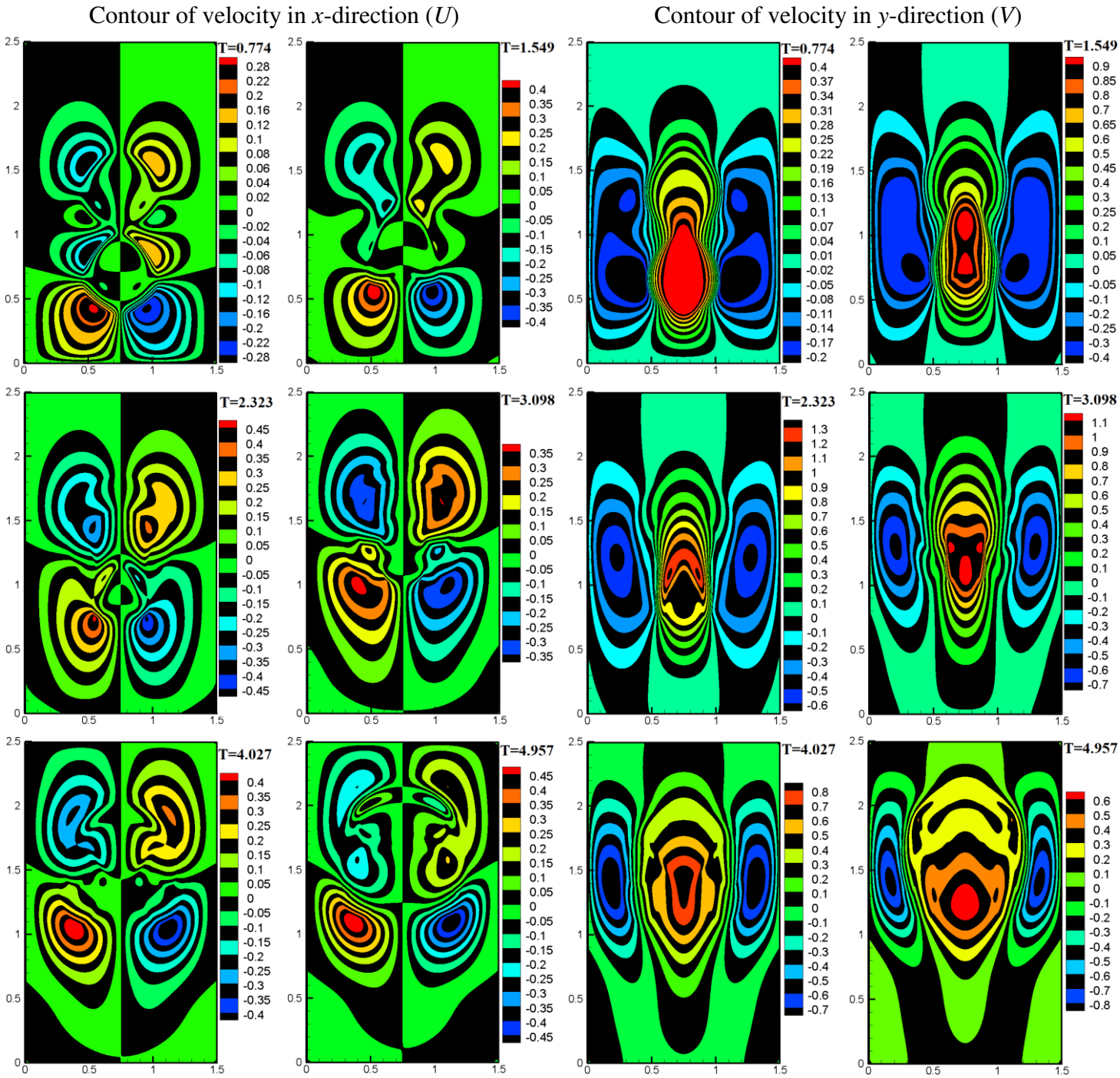

Fig. 22. Transient evolution of non-dimensional velocity components in x and y-directions ($U = u/\sqrt{2gR}$, $V = v/\sqrt{2gR}$) in case 9 at different non-dimensional time instants ($T = t\sqrt{g/(2R)}$).

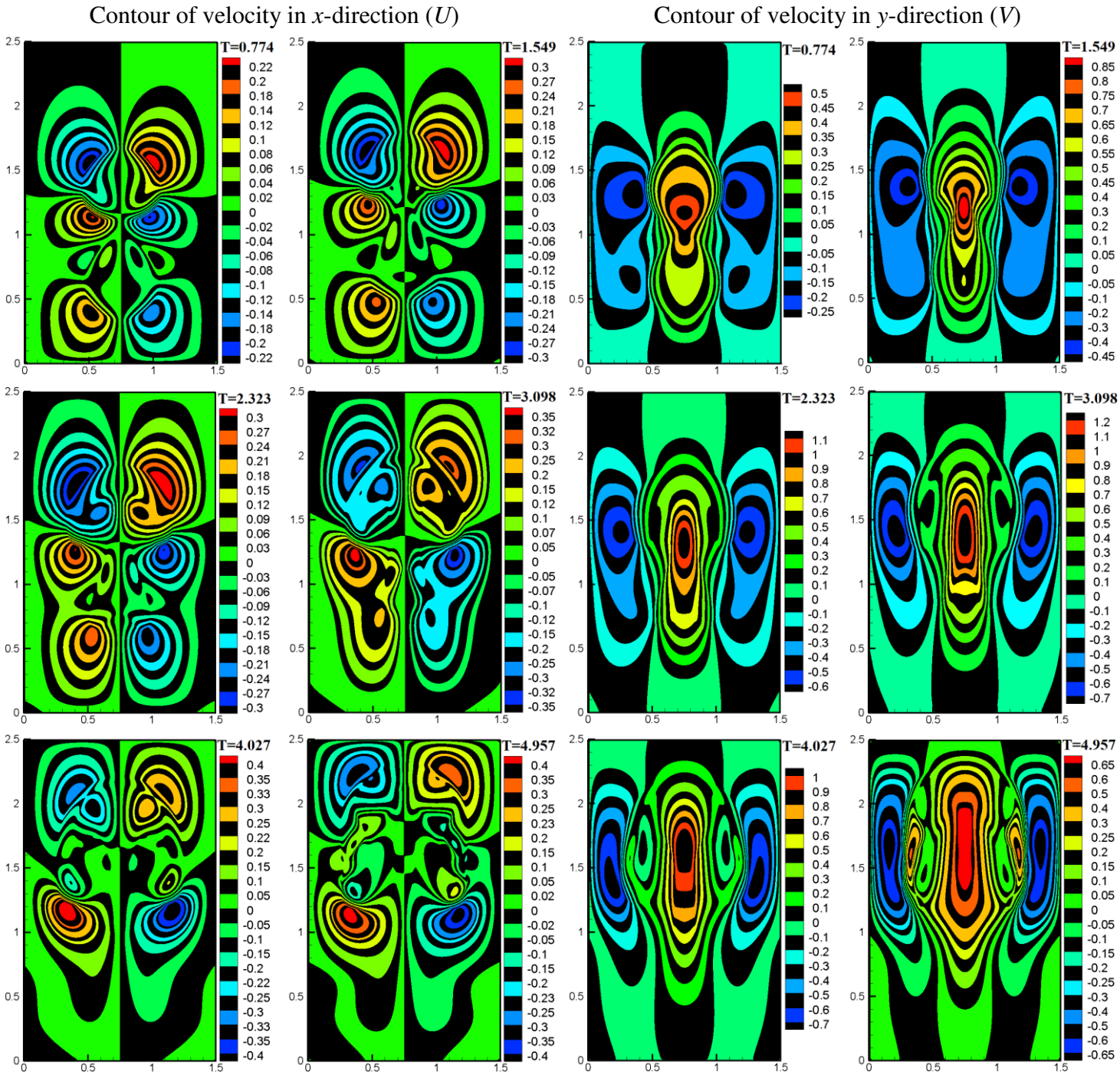

Fig. 23. Transient evolution of velocity components in x and y-directions ($U = u/\sqrt{2gR}$, $V = v/\sqrt{2gR}$) in case 10 at different non-dimensional time instants ($T = t\sqrt{g/(2R)}$).

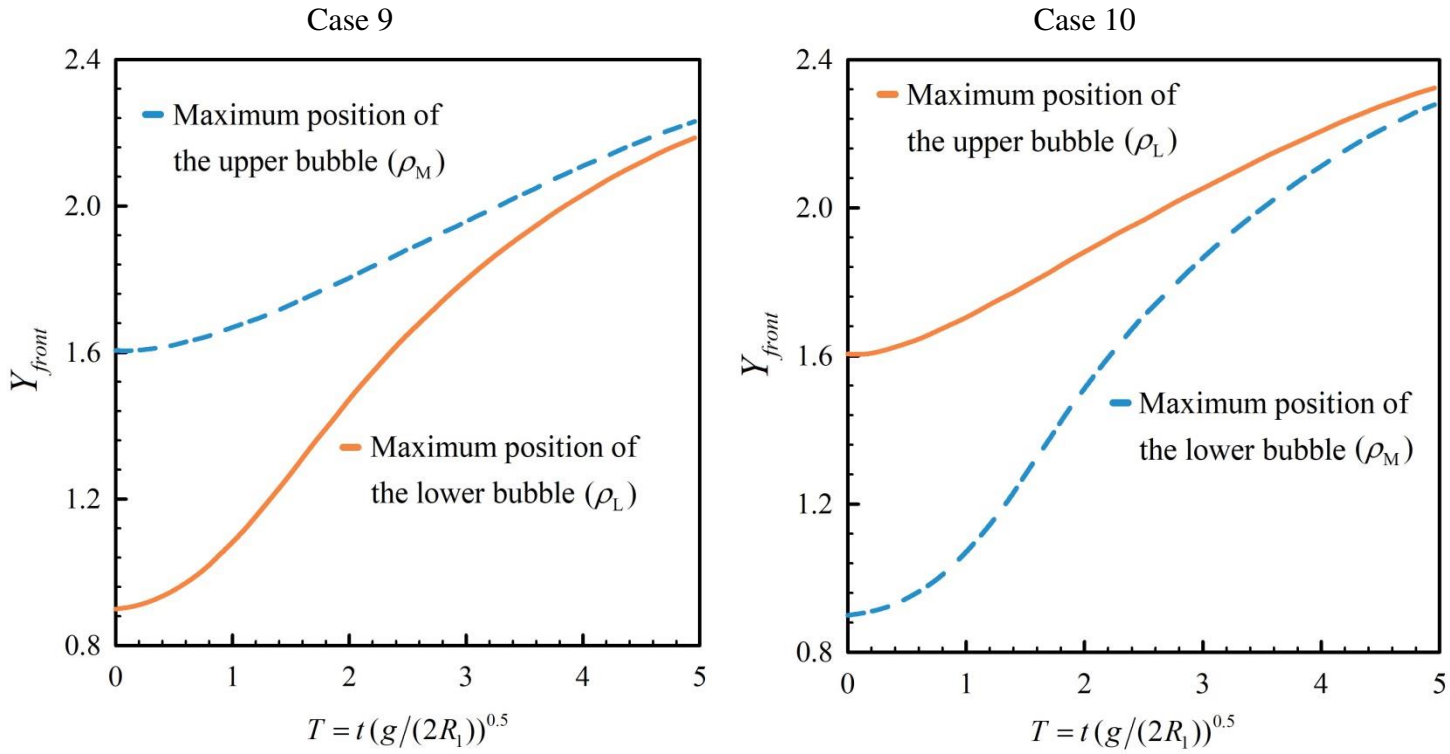

Fig. 24. Time histories of maximum locations of the bubbles fronts (Y_{front}) in cases 9 and 10.

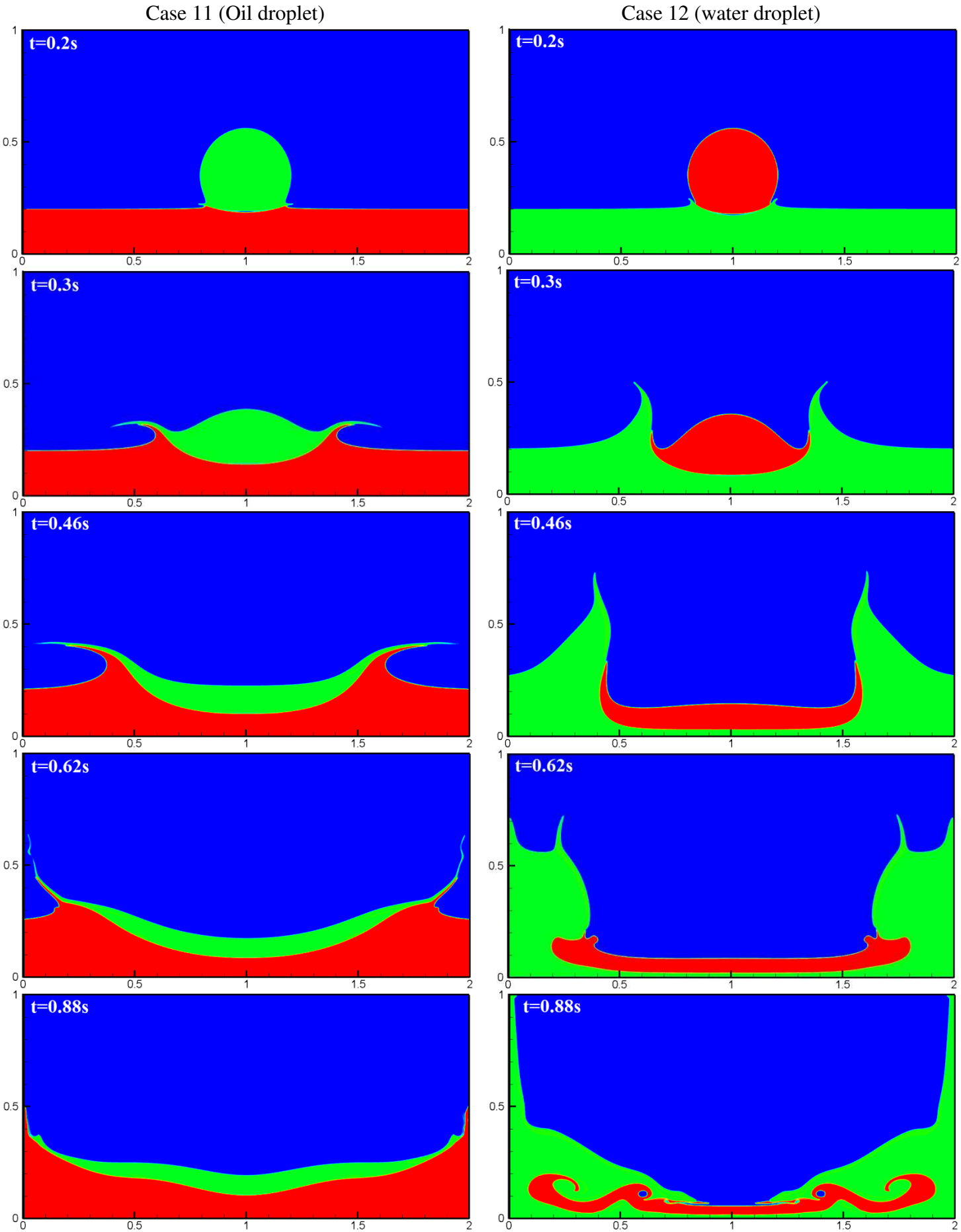

Fig. 25. Transient evolution of droplets impacting on the wet beds in cases 11 and 12 at different time instants.

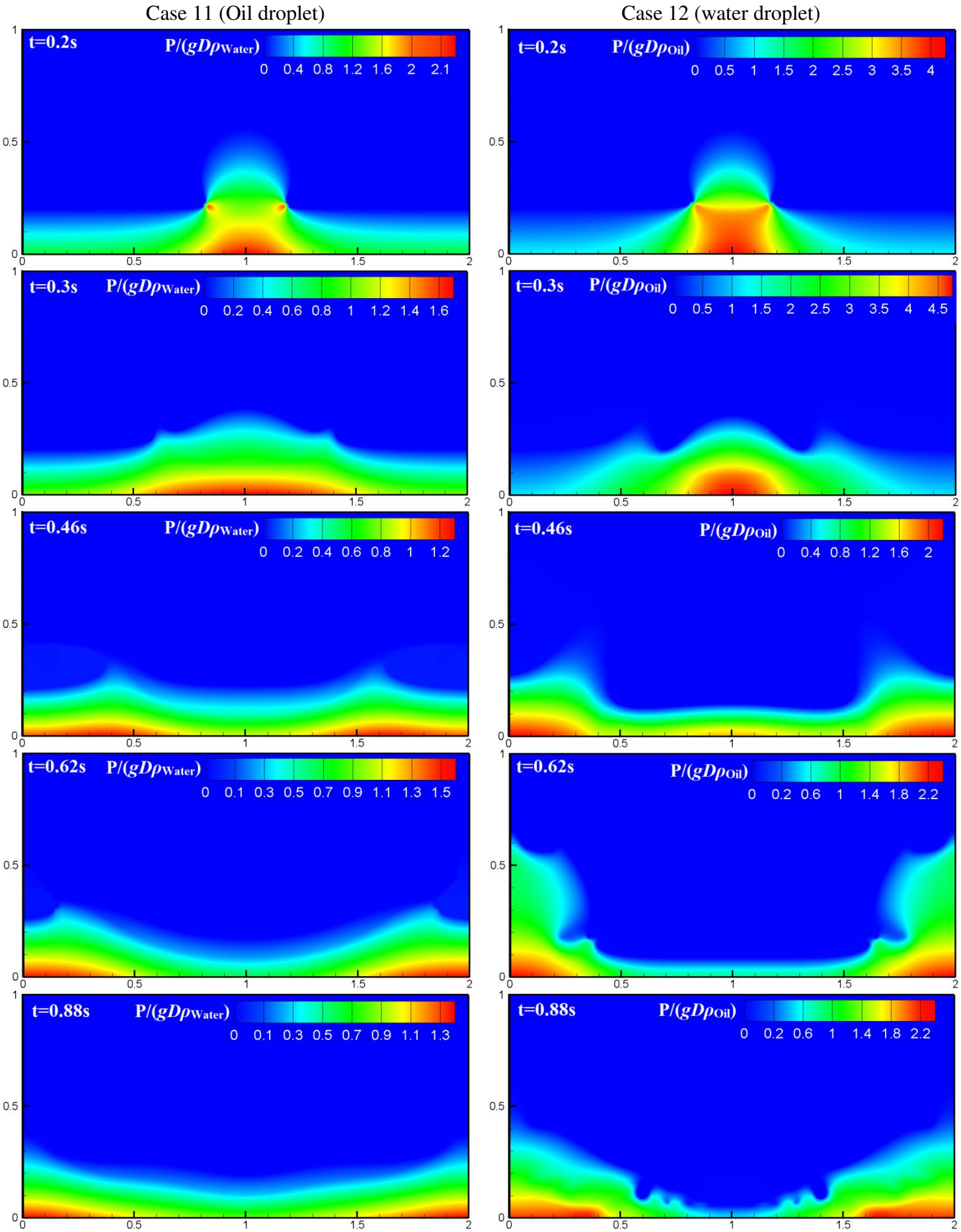

Fig. 26. Transient variation of pressure fields in cases 11 and 12 during the droplets impacting.

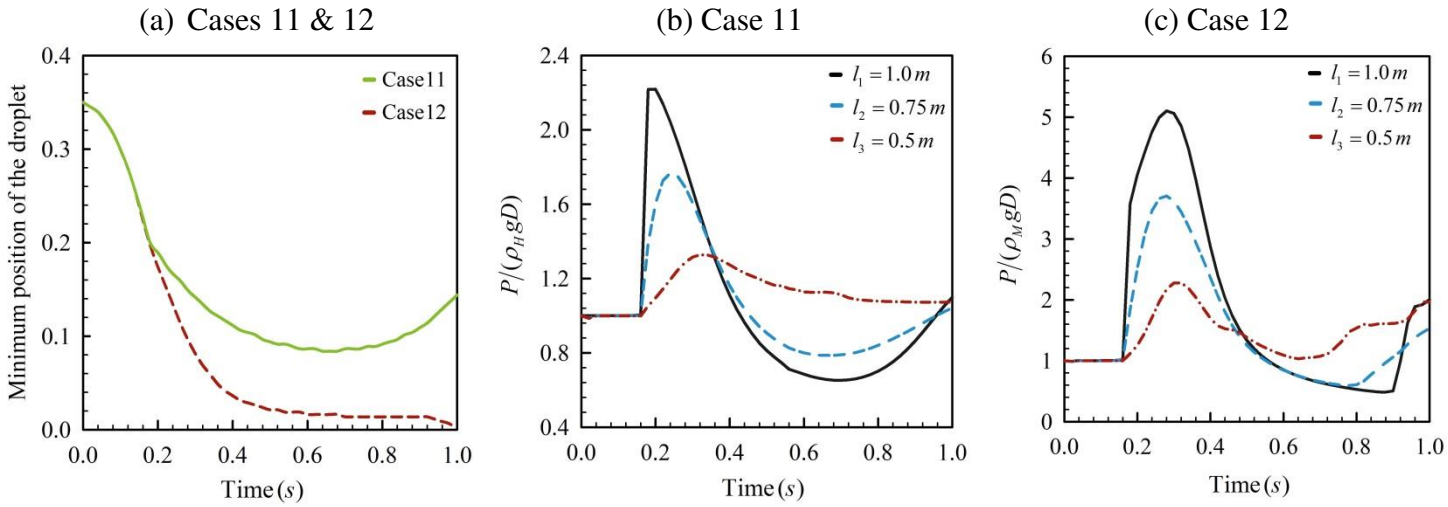

Fig. 27. (a) Time variations of minimum position of the droplets in cases 11 and 12 and (b)-(c) time histories of pressure variation on the bottom wall at three different marked points in cases 11 and 12 (l_1=1.0 m, l_2=0.75 m and l_3=0.5 m).